Kobe University Repository : Kernel

PDF issue: 2024-09-23

Enhanced and Asymmetric Melting Beneath the Southern Mariana Back-Arc Spreading Center Under the Influence of Pacific Plate Subduction

Matsuno, Tetsuo

Seama, Nobukazu

Shindo, P. Haruka

Nogi, Yoshifumi

Okino, Kyoko

(Citation)
Journal of Geophysical Research: Solid Earth,127(3):e2021JB022374

(Issue Date)
2022-05-05

(Resource Type)
journal article

(Version)
Accepted Manuscript

(Rights)
© 2022. American Geophysical Union. All Rights Reserved.
This is the peer reviewed version of the following article: Matsuno, T., Seama, N., Shindo, H. P., Nogi, Y., & Okino, K. (2022). Enhanced and asymmetric melting beneath the southern Mariana back-arc spreading center under the influence of Pacific plate…

(URL)
https://hdl.handle.net/20.500.14094/0100477907

Enhanced and asymmetric melting beneath the southern Mariana back-arc spreading center under the influence of Pacific plate subduction

Tetsuo Matsuno[1], Nobukazu Seama[2,1], Haruka P. Shindo[2], Yoshifumi Nogi[3], Kyoko Okino[4]

1. Kobe Ocean-Bottom Exploration Center (KOBEC), Kobe University, Kobe, Japan
2. Department of Planetology, Kobe University, Kobe, Japan
3. National Institute of Polar Research/Department of Polar Research, The Graduate University for Advanced Studies (Sokendai), Tokyo, Japan
4. Atmosphere and Ocean Research Institute, The University of Tokyo, Chiba, Japan

corresponding author: Tetsuo Matsuno
Email: matsuno@port.kobe-u.ac.jp
ORCID: https://orcid.org/0000-0002-2475-4427
Tel: +81-78-431-4620

Key points

- We obtain an electrical resistivity structure model of the upper mantle at 13°N in the southern Mariana Trough.
- The model reveals the distribution of melt and water (or hydrogen) and the mantle dynamics in this back-arc basin.
- The model suggests the enhanced and asymmetric melting beneath the spreading center under the influence of the Pacific plate subduction.

Abstract

The back-arc spreading at the southern Mariana is categorized as slow, but surface morphological and geophysical features of the spreading centers suggest that the spreading process is associated with enhanced melting in the upper mantle, due to water being derived from the subducted Pacific slab. A marine magnetotelluric experiment was performed along a transect across a segment at 13°N to reveal the key processes of melting, dehydration, and dynamics in the upper mantle, and their relationships to the surface characteristics. Our inversion model of electrical resistivity shows (1) a conductive body at 10-20 km depth beneath the spreading axis, and (2) another conductive area expanding asymmetrically under and around the conductive body. Away from the spreading center, there is (3) a resistive area thickening up to ~40 km on the remnant arc side, and (4) another resistive area with a constant thickness of ~150 km on the trench side. Implications of these model features are (1) a melt body beneath the spreading axis; (2) a hydrous mantle above the subducted slab and asymmetric passive decompression melting in the mantle wedge; (3) a residual mantle off from the spreading axis; and (4) a cold mantle wedge tip and the subducted Pacific mantle. The structure markedly contrasts with that in the central Mariana Trough at 18°N, suggesting that the horizontal distance between the location of the spreading center and the root of the buoyant upwelling above the subducted slab is a key parameter that controls the mantle dynamics beneath the back-arc spreading.

Plain language summary

The seafloor spreading has occurred at the southern Mariana Trough due to the subduction of the Pacific plate beneath the Philippine Sea plate, and its spreading rate has been considered to be slow. However, geophysical features of the seafloor suggest a larger amount of melt in the upper mantle than expected from the spreading rate. To investigate this, an electromagnetic survey was conducted to determine the electrical resistivity structure of the upper mantle beneath the southern Mariana Trough. This survey helps by providing information on the thermal structure, the distribution of melt and water. The survey found a small conducting body beneath the spreading center, a larger conductive area under and around this, and two resistive areas away from the spreading center. This structure in the southern Mariana Trough is different from that in the central Mariana Trough. We attribute this to the subduction of the Pacific plate that has led to a higher melt production in the upper mantle in the southern Mariana Trough. Our results suggest that the horizontal distance between the location of the spreading center and the melting area above the subducted plate is a key parameter for the mantle dynamics beneath the back-arc spreading.

1. Introduction

A prominent result of past studies of mid-ocean ridge systematics is the identification of the positive relationship between the seafloor spreading rate and melt production beneath the ridge. This relationship influences the seafloor morphology, gravity anomaly distribution, crustal volume, the production rate of partial melt, the shape of the melting regime in the mantle, and the mantle upwelling pattern (Macdonald et al., 1991; Forsyth, 1992). Recent observational studies on both mid-ocean ridges and back-arc spreading centers have revealed that these features are highly diverse and exhibit deviations from this relationship (e.g., Dalton et al., 2014; Dunn and Martinez, 2011). The deviations suggest more or less melt production beneath the ridge than expected from the seafloor spreading rate. The reasons for the deviations include thermal, compositional, and geochemical heterogeneities in the mantle sources, which can be produced by hotspot upwelling, ancient differentiation of the mantle under mid-ocean ridges (Dalton et al., 2014; Ito et al., 2003; Liu et al., 2008), and plate subduction. Plate subduction leads to dehydration of the subducted slab, hydration and melting of the overlying mantle wedge, and interactions of melting regions beneath an arc and a back-arc spreading center (Martinez and Taylor, 2002; Dunn and Martinez, 2011).

The melt production beneath the back-arc spreading center in the southern Mariana Trough is higher than expected from its spreading rate and differs from those beneath the other spreading centers in the Mariana Trough (e.g., Martinez et al., 2000; Kitada et al., 2006; Seama et al., 2015). The full seafloor spreading rate in the southern Mariana Trough was 46 mm/yr in the past (Seama and Okino, 2015) and remains similar in the present (Kato et al., 2003). This spreading rate is the fastest within the whole basin (Martinez et al., 2000; Seama and Okino, 2015; Kato et al., 2003) but is still categorized as slow in the global mid-ocean ridge system (Macdonald et al., 1991). Despite its slow spreading rate, the southern Mariana Trough exhibits characteristics that are usually observed at fast-spreading centers in the East Pacific Rise (EPR), including axial-high or inflated ridge morphology, a constant low gravitational anomaly along the axis, a thick crust inferred from gravitational data, and a melt lens in the crust (Martinez et al., 2000; Kitada et al., 2006; Becker et al., 2010). These observations suggest that the melt production rate and its total amount beneath the southern Mariana back-arc spreading centers are high and that mantle upwelling occurs in the sheet-like style that is typical of fast-spreading centers rather than in the focused or diaper upwelling style that is typical of slow-spreading centers (Lin and Morgan, 1992; Kitada et al., 2006).

One hypothesis for the cause of the high melt production beneath the southern Mariana back-arc center is that the melting process beneath the spreading center is influenced by Pacific slab-derived fluid that under other circumstances would generate an arc chain (Martinez et al., 2000; Stern et al., 2013; Seama et al., 2015). Some observations, including an estimate of the 1-D crustal seismic velocity structure (Sato et al., 2015) and the geochemistry of rock samples from the ridge (Taylor and Martinez, 2003; Pearce et al., 2005; Masuda and Fryer, 2015), suggest the influence of slab-derived water and arc-related geochemical components on the melting process. In a map of the slab surface at depth, the depth contours of 100-150 km (Hayes et al., 2012) cross the back-arc spreading ridge known as the Malaguana-Gadau Ridge (MGR) in the southern Marianas (Figure 1), whereas the same contours are coincident with the location of the currently active arc volcanic front in the crescent-shaped northern and central Marianas (Figure 1). The chain of subaerial and submarine arc stratovolcanoes actually terminates at the Tracey seamount at 13°40'N (Stern et al., 2013), but there are volcanic edifices in the seamount chains of the Fina Nagu Volcanic Chain (FNVC) and the Patgon-Masala Volcanic Chain (PMVC) off the MGR, which could be small arc volcanoes (Figure 1) (Stern et al., 2013; Masuda and Fryer, 2015; Brounce et al., 2016). The partial melting process beneath back-arc spreading centers and arcs, as well as dehydration-hydration reactions in subduction zones, is known to be the composite result of multiple factors, such as pressure, thermal structure, characteristics (age, velocity, morphology) of the subducting plate, mantle flow, grain size, melt and water permeability, dehydration reactions of hydrous minerals (e.g., Tatsumi, 1986; Schmidt and Poli, 1998; Hacker, 2003; Sdrolias and Müller, 2006; Cagnioncle et al., 2007; Grove et al., 2009; England and Katz, 2010; van Keken et al., 2011; Wilson et al., 2014; Wada and Behn, 2015). Therefore, identifying mantle structures that reflect complex melting and dehydration-hydration processes is a key to understanding the mantle dynamics of the southern Mariana Trough and its relevance to other observations that suggest high melt production and the interaction of melting regimes in the same area.

In this paper, we present a result of a marine magnetotelluric (MT) experiment across a back-arc spreading segment at 13°N in the southern Mariana Trough. Based on the results of the experiment, we reveal the electrical resistivity structure of the upper mantle. The resistivity structure was estimated from an analysis of ocean bottom MT transect data. Because the electrical resistivity of the upper mantle is primarily dependent on temperature, the amount of partial melt interconnected, and the amount of water (or hydrogen) dissolved in background solid phase mantle (we mainly consider olivine in this study) and in melt, our electrical resistivity structure presents observational evidence on the thermal structure, the distribution and the amount of melt and water, and the melting processes beneath the back-arc spreading ridge and on the dehydration-hydration processes in the mantle wedge in the southern Mariana Trough, all of which are expected to be under the influence of Pacific plate subduction.

2. Observation and data

We conducted a marine MT experiment across the MGR at 13°N in the southern Mariana Trough along an ~120-km-long WNW-ESE transect (Figure 1) from August to October 2010. We used 11 ocean bottom electromagnetometers (OBEMs) for the experiment and successfully recovered 10 of the 11 OBEMs (Figure 1 and Table 1). The OBEMs measured three components of the time-varying electromagnetic field and two components of the instrumental tilt at the seafloor at 60-s intervals for 40-80 days. The deployment and recovery of the OBEMs were conducted during the cruises YK10-10 and YK10-15, respectively, of the *S/V Yokosuka*, operated by the Japan Agency for Marine-Earth Science and Technology (JAMSTEC).

We checked and corrected the time-varying electromagnetic field data for spikes and steps. The clock drifts of the OBEMs were determined to be <60 s, and we corrected the drifts by assuming a linear trend. Instrumental tilts were <20° for almost all instruments, and we corrected the instrumental tilts using the tilt data observed. The OBEMs are usually tilted at seafloor, and MT responses estimated from data with the tilted OBEMs may be different from those in horizontal plane if the tilt is not corrected. We correct the tilt of the OBEMs using the two-components tilt data by 3-D rotation according to Rodrigues' rotation formula. After the tilt correction, directions of the instruments in the horizontal plane were estimated by comparing the observed magnetic field with the IGRF-12 geomagnetic model field (Thebault et al., 2015). The electric field data at EM5 and EM11 stations were quite noisy, and thus, these data were not used in further data analyses. Line spectra were found at periods of 10^4-10^5 s, which were related to solar quiet (Sq) daily variations in the external magnetic field and oceanic tides (Shimizu et al., 2011). These line spectra were removed by applying robust least-square fitting of sine functions at known frequencies of Sq variations (as well as their higher harmonics up to three) and oceanic tides to the original time-series data.

3. MT response function

3.1. Estimation of MT response function

We estimated an MT response function at each station from the data processed as described above at each station through the bounded influence, remote reference (BIRRP) algorithm (Chave and Thomson, 2004). The electric field data used to estimate the MT responses at the stations EM5 and EM11 were from the stations EM8 and EM10, respectively (Table 1), based on the total data lengths, closeness of the stations, and noise in the electric field data. The locations of the EM8 and EM10 stations were taken into account in forward modeling and inversion, which are described in the following sections, for the use of these electric field data for the EM5 and EM11 responses. Remote reference stations were selected by considering remoteness of stations, noise in the magnetic field data, and improvement of the estimated MT responses based on the remote reference (Table 1). We determined a final MT response set after checking the diagnostic outputs of the BIRRP program and variations in the response as a function of period, which should be physically smooth. At this stage of the response selection, the EM4 response was excluded from the data set because of low squared coherences between the observed and predicted electric fields. The x-axis of the coordinate system for the responses was set to N35°E, which is parallel to the ridge strike, so the y-axis is parallel to the seafloor spreading direction.

3.2. Correction for topographic distortions

Marine MT responses are usually distorted by electric currents generated by the contrast between conductive seawater and resistive subseafloor structures through rugged seafloor topography and coast line geometry (e.g., Baba and Chave, 2005). Without consideration of such topographic distortions, the marine MT responses cannot accurately be interpreted when investigating target structures (e.g., Baba and Chave, 2005). One method to eliminate the influence of topographic distortions is a correction method, in which correcting an observed MT impedance tensor based on a distortion equation that relates a distorted impedance tensor to an undistorted impedance tensor (e.g., Nolasco et al., 1998; Baba and Chave, 2005; Matsuno et al., 2007).

We corrected topographic distortions using the equation of Nolasco et al. (1998), which is

$$\mathbf{Z}_{cor}(\mathbf{r},\omega) = [\mathbf{I} - \mathbf{M}(\mathbf{r},\omega)][\mathbf{I} - \mathbf{Z}_{obs}(\mathbf{r},\omega)\mathbf{K}(\mathbf{r},\omega)]^{-1}\mathbf{Z}_{obs}(\mathbf{r},\omega) \quad (1).$$

In this equation, $\mathbf{Z}_{cor}$ is an MT impedance corrected for topographic distortions, $\mathbf{Z}_{obs}$ is an observed MT impedance, $\mathbf{M}$ and $\mathbf{K}$ are 2 by 2 complex-valued matrices representing topographic distortions in the horizontal electric and magnetic fields, respectively, $\mathbf{I}$ is the same-order identity matrix, $\mathbf{r}$ represents a location in the Cartesian coordinate system ($\mathbf{r} = (\mathrm{x}, \mathrm{y}, \mathrm{z})$), and ω is an angular frequency. The $\mathbf{M}$ and $\mathbf{K}$ matrices are calculated from

$$\mathbf{E}_{topo,h}(\mathbf{r},\omega) = \mathbf{E}_{flat,h}(\omega) + \mathbf{M}(\mathbf{r},\omega)\mathbf{E}_{topo,h}(\mathbf{r},\omega) \quad (2)$$

and

$$\mathbf{B}_{topo,h}(\mathbf{r},\omega) = \mathbf{B}_{flat,h}(\omega) + \mathbf{K}(\mathbf{r},\omega)\mathbf{E}_{topo,h}(\mathbf{r},\omega), \quad (3)$$

respectively. These equations relate the horizontal electric and magnetic fields with and without distortions, and the subscripts *topo* and *flat* indicate field components with and without topographic distortions, respectively. The horizontal electric and magnetic fields with the subscripts *topo* and *flat* are calculated with the Flattening Surface 3-D modeling program (Baba and Seama, 2002) without and with surface 3-D topography, respectively. The horizontal area of the 3-D forward modeling was 4380 km × 4460 km in the x- and y-directions, respectively, which covered a part of the Eurasia Continent, and the depth range of the 3-D forward modeling (z-direction) is 1690 km. The bathymetric and topographic data are derived from a multi-narrow beam data set (Kitada et al., 2006) and the ETOPO1 data (Amante and Eakins, 2009). The horizontal block size was a minimum of 1 km^2 near the stations and coarser away from the stations. The water depth of the flat seafloor in the MT responses after topographic correction was set to 3500 m, which was an approximation of the average station water depth (Table 1). The subseafloor electrical resistivity structure consisted of a two-layer 1-D model and a 3-D subducted Pacific slab. The two-layer 1-D model represented an oceanic lithosphere-asthenosphere structure, and the resistivity of the upper layer was 3×10^3 Ω-m, and that of the underlying half-space was 3×10^1 Ω-m. The surface of the 3-D subducted slab was derived from the slab geometry data of Slab1.0 for the Izu-Bonin-Marianas (Hayes et al., 2012). The thickness of the slab was assumed to be 100 km, and the resistivity of the subducted slab was assumed to be 3×10^3 Ω-m. The correction equation of Nolasco et al. (1998) is relatively robust to subseafloor structures (Matsuno et al., 2007). Additionally, to enhance the correctness of the topographic correction (or to make observed MT impedances closer to "real topographic distortion-free" impedances by the correction), we introduce the obvious regional 3-D slab structure into the forward modeling for the correction.

We checked the validity of the topographic correction in this manner through a synthetic test (see Text S1.1. and related figures in the supporting information), and the result showed that the correction is robust. We also checked the coupling between the surface bathymetry and the subseafloor electrical resistivity structure in the topographic correction by repeating the topographic correction of the observational responses using the optimal 2-D inversion model and the 3-D slab model (Text S1.1. and related figures in the supporting information). From the results, we concluded that the topographic correction effectively produces distortion-free MT responses.

The apparent resistivities and phases before and after the topographic correction are shown in Figure 2 and Figure 3, respectively. Large differences before and after the correction were found in off-diagonal elements at the easternmost two stations, EM10 and EM11. These two stations were located between the topographic high of the FNVC and the topographic low of the West Santa Rosa Bank Fault (WSRBF) and were closer to the modern and Eocene frontal arc high and the Mariana Trench deep than the other observational stations (Figure 1). The amplitudes of the diagonal elements of the apparent resistivity after the correction were smaller than those before the correction by 1-2 order of magnitude (Figure 2). Polarization diagrams of the responses as a function of period and station before and after the topographic correction are shown in Figure S1. The off-diagonal element shows circle or eclipse with the major axis that is perpendicular or parallel to the transect direction and the size or radius of the off-diagonal element is larger than that of the diagonal element at almost all periods and stations. Some diagrams such as those at $\leq$2560 s and at EM10 imply strong 3-D structural effects and/or topographic distortions that are not removed by the correction, and these impedances will be removed in the robust inversion processing described in section 4.

4. Two-dimensional inversion

4.1. Method

We obtained 2-D electrical resistivity models beneath the transect through a nonlinear conjugate gradient inversion algorithm (Rodi and Mackie, 2001). This inversion algorithm is originally used for exploring not only an isotropic model but also an anisotropic model. In this study, we explored only isotropic models by setting the regularization parameter for model anisotropy (Baba et al., 2006) to 100 that forces the inversion model obtained to be isotropy (Baba et al., 2006; Matsuno et al., 2010). The model range of the inversions was 2600 km × 1110 km in the y- and z-directions, respectively, which sufficiently covered the transect length (~130 km). The element size for the inversion model was a minimum of 500 m × 500 m near the stations and was coarser away from the transect. An initial model for inversion was a homogeneous 10^2 Ω-m. Error floors were assigned to 10% for apparent resistivity and 2.85° for phase. Both values correspond to 5% of the MT impedance magnitude. These error floors are effective for the data, whose minimum error is 8.7% and typical error range is 9-30% for apparent resistivity, and whose minimum error is 2.49° and typical error range is 3°-9° for phase, respectively. Those error floors are set to be consistent with those used for the central Marianas study of Matsuno et al. (2010).

In the inversion, we set a model smoothing operator to be a uniform Laplacian grid and set a penalty function for model smoothness to minimize the square of the Laplacian model parameters. There are other parameters controlling model smoothness in the inversion program, α and β, which potentially have large impacts on the resultant inversion models at subduction zones (Matsuno et al., 2010). We systematically tested several values for α and β and finally set α = 1.0 and β = 1.7; the same parameter set was used by Matsuno et al. (2010) in an analysis of central Marianas MT data. These α and β values were fixed in all subsequent inversion processing.

We used only the TM mode responses for the 2-D inversion and thus checked its validity through 3-D forward modeling and inversion. Based on the seafloor topography around the MT transect and the subducted Pacific slab seismically imaged beneath the transect (Miller et al., 2006; Hayes et al., 2012), we expected the electrical resistivity structure to be dominantly 2-D near the transect and 3-D away from the transect. The 2-D structure is likely related to the back-arc spreading process, and the 3-D structure is likely related to the subduction process. To check the validity of using the 2-D inversion of only TM mode responses from 2-D transect data to investigate possible 3-D resistivity structures, we conducted synthetic forward modeling and inversion tests. We concluded that the 2-D inversion models obtained in the manner we applied to the observed data represent the main features of a possible 3-D electrical resistivity structure. Further, we carry out a 3-D inversion with the observed MT impedances using a program of Usui (2015) and Usui et al. (2018), even though the data set may not be suitable for 3-D inversion because the MT impedances are available only along the transect (Figure 1). Details of the 3-D inversion are described in the supporting information. The 3-D inversion model along the transect (Figure S11) is fundamentally similar to the 2-D inversion result shown below. Details of the forward modeling and inversion tests are described in the supporting information. The behaviors of MT impedances and polarization diagrams after the topographic correction, the synthetic test of 3-D forward modeling and 2-D inversion for the plausible 3-D model, and the 3-D inversion of the real data set that is limited along the transect support that our 2-D treatment of the data set. This conclusion is consistent with results of previous studies showing that the TM mode response is less affected by off-transect resistivity anomalies (Wannamaker et al., 1984; Ledo et al., 2002).

We applied a robust inversion algorithm (Matsuno et al., 2014) to obtain the electrical resistivity structure by removing statistical outliers in the inversion data set. The robust run of the algorithm (i.e., detection and removal of outliers and subsequent inversion with a culled data set) was repeated two times. Some of the data from EM10 were judged to be outliers and were removed by the robust processing. The values of the regularization parameter of model smoothness (τ_s) tested in the robust runs were 300, 100, 30, 10, 3, 1, 0.3, 0.1, and 0.03, and three L-curves were obtained (Figure 4a). Based on these L-curve tests, we determined that the inversion model for $\tau_s = 0.3$ in the second robust run was optimal. A quantile-quantile plot of the TM mode response for this optimal inversion model showed no outliers, and the normality of the residual distribution was within the 95% confidence limit (Figure 4b).

We obtained two types of 2-D electrical resistivity models; 1) a model with a constraint only on model smoothness, and 2) a model not only with the constraint on model smoothness but also with an allowance for resistivity jump along the boundary delineating the subducted Pacific slab (Figure 5). The robust inversion iteration described above was conducted for the type 1) and Figure 4 is a plot for this type. We did not independently apply the robust inversion process to obtain the type 2) model. We obtained the final data set that was obtained in the robust inversion process for obtaining the type 1) model, and this final data set was used to obtain the type 2) model. We confirmed that the optimal τ_s value for the type 1) model is also optimal for the type 2) model, and that outliers were not found for the type 2) model as similar to the type 1) model. MT data are usually not sensitive to high-resistivity bodies, such as subducted slabs, especially those elongated vertically, as shown by the inversion of central Mariana data (Matsuno et al., 2010). Inversion with the allowance for a resistivity jump at the subducted slab boundary improves imaging of electrical resistivity structures in subduction zones (Matsuno et al., 2010; Evans et al., 2013; McGary et al., 2014). The boundary of the slab surface was derived from data from the Slab1.0 model (Hayes et al., 2012), and the location of the slab bottom was obtained by assuming that the slab thickness is 100 km. The tip of the slab was set at 200 km depth based on the Slab1.0 model (Hayes et al., 2012). We note that the resistivity of the slab was not given *a priori*.

4.2. Results

Figure 5 presents two types of optimal 2-D inversion models and Figure 6 shows the predicted TM mode responses for the models and the observed responses after topographic correction. The predicted responses of both types of inversions are almost identical to the observations, as evidenced by a root mean square (RMS) misfit of 1.13 without the slab constraint and 1.14 with the slab constraint (Figure 6 and Tables S1 and S2).

There are four notable features in the inversion models (Figure 5). The first model feature is a horizontally elongated low-resistivity area ($10^{0.8}$-$10^{1.4}$ Ω-m) at depths of 5-20 km beneath the spreading center (C1). This shallow flat-shaped conductive area offsets from the spreading center toward the trench side. The eastward extension of the conductive area is constrained by the data from the EM10 station, and the westward extension is constrained by the data from the EM5 station. There is a vertically elongated conductor (~$10^{1.3}$ Ω-m) below and connected to this shallow conductive body. The second model feature is a moderately low-resistivity area ($10^{1.2}$-10^2 Ω-m) expanding asymmetrically with a wider area on the remnant arc side and a sharp vertical discontinuity on the trench side (C2). This moderately conductive area, which includes the vertical conductor connected to the shallow flat conductor, generally becomes more conductive with depth. Corresponding to the presence of the asymmetric moderately conductive area, two high-resistivity areas (>10^3 Ω-m) with different shapes exist away from the ridge center on the remnant arc side (R1) and on the trench side (R2), respectively. The third model feature is the resistive area on the remnant arc side that thickens from the ridge center up to ~40 km beneath the easternmost station (R1). The fourth model feature is the resistive area on the trench side that has a thickness of up to ~150 km (R2).

4.3. Data sensitivity to the inversion model

We check the sensitivity of the MT responses to the entire 2-D inversion model. The sensitivity was first investigated with the squared diagonal of a matrix product from a Jacobian matrix and a covariance matrix for data error (Figure S12; Baba et al., 2006). This sensitivity map shows high sensitivity of the data to the mantle wedge structure, suggesting that the mantle wedge structure is constrained well by the data. The map shows low sensitivity values in the subducted slab underlying the mantle wedge, where the resistivity of the subducted slab decreases from the trench to the ridge center (Figure 5). The insensitivity is possibly due to the low sensitivity of the MT responses to the resistive slab under the conductive mantle wedge.

We also check the sensitivity of the MT responses to some notable model features, especially at shallow depths. A shallow conductor beneath the spreading center, which is located at depths of 5-20 km and a distance of approximately +10 km and has a flat shape (Figure 5) has a large impact on MT responses. We conduct a forward modeling test by changing the resistivity of the conductor to be more resistive in a rectangle area (at 5-15 km depth and at 0-40 km distance) and see changes in the total RMS misfit. If the resistivity of this area (the rectangle area at 5-15 km depth and at 0-40 km depth) is uniformly changed to 3×10^1 Ω-m, the total RMS misfit becomes large as 1.29. RMS misfit changes are large at sites between EM4 and EM11 except for EM10 over the area

(5-50% increase), and those are larger at shorter periods and are found at the longest period of 61440 s (10-60% increase). This result suggests this shallow depth area should be conductive with a value of ~10 Ω-m. We conduct further tests on the sensitivity to the shallow conductor, because the study on the central Mariana Trough indicates that a conductor in some shape at depths of 6-60 km affect MT responses only at the periods shorter than 1000 s (Matsuno et al., 2012). We have MT responses at $<10^3$ s at the EM5 and EM8 stations above the shallow conductor in the inversions (Figure 6). We check the influence of these short-period responses on the result by excluding them from the inversion data set. The resultant inversion models similarly showed the shallow conductor with a minimum resistivity of $10^{1.0}$ Ω-m (Figure S13), which is slightly higher than the minimum resistivity of $10^{0.7}$ Ω-m observed in the inversion using all the short-period responses (Figure 5a), but the change in the RMS misfit was not significant (1.17 in the model shown in Figure S13 vs. 1.13 in the model shown in Figure 5a). This inversion test supports that the shallow conductor is constrained not only by the short period ($<10^3$ s) responses but also responses at longer periods ($>10^3$ s) and at other sites.

The existence of the vertically elongated conductor under the shallow flat conductor (Figure 5) was tested by forward modeling, because the MT data could be insensitive to the underlying vertical conductor. The forward modeling test is conducted by changing the resistivity to 10^2 Ω-m in a rectangle area of 25-70 km depth and -5-15 km distance. The total RMS misfit increased to 1.29. RMS misfit changes becomes large relatively evenly at all the sites except for EM2 (5-20% increase), and those are larger at long periods of 5120-35110 s (10-25% increase). This result suggests that the conductor is required by the observed MT responses.

The shallow flat-shaped conductor and the underlying vertical conductor together seem to be slightly offset toward the trench side by ~5-10 km distance in the inversion models (Figure 5). We also carried out an inversion test focusing on the horizontal location of the vertical conductor (Figure S14). The result of the inversion test suggests that the vertical conductor is not necessarily offset toward the trench side and could be located immediately beneath the ridge center with its center at ~0 km distance (this pattern might result from the number and the arrangement of data stations) but would not be located at a negative distance location (i.e., toward the remnant arc side) (Figure S14).

5. Discussion

We restate the four remarkable features in the inversion models (Figure 5): (1) a conductive area at 10-20 km depth beneath the spreading axis, whose position is slightly offset from the spreading axis toward the trench side, (2) a moderately conductive area expanding asymmetrically under and around the conductive area of (1), (3) a resistive area thickening from the ridge center up to approximately 40 km on the remnant arc side, and (4) a resistive area with a constant thickness of approximately 150 km on the trench side. In the following discussion, we conclude that these model features suggest that there is (1) a melt body beneath the spreading axis; (2) a hydrous mantle wedge produced by dehydration of the subducted Pacific slab and asymmetric passive decompression melting in the mantle wedge, (3) a residual lithospheric mantle off the spreading axis, and (4) a cold mantle wedge tip and the subducted Pacific lithospheric mantle. Furthermore, we discuss our inversion models in terms of relevance to other observations in the southern Mariana Trough and compare our results with the electrical resistivity structure of the upper mantle in the central Mariana subduction system (Matsuno et al., 2010, 2012).

5.1. Melting and hydration beneath the back-arc spreading center and in the mantle wedge

The shallow conductor beneath the ridge center ($10^{0.8}$-$10^{1.4}$ Ω-m) is not simply due to high temperatures but requires a melt body that can contain water. The resistivity of melt-free dry olivine at a temperature of approximately 1350°C, which is the average potential temperature of the Mariana Trough (Kelley et al., 2006; Wiens et al., 2006), is $\geq 10^2$ Ω-m (Figure 7a) (Constable et al., 1992; Constable, 2006; Yoshino et al., 2009; Gardés et al., 2014). This resistivity value is much higher than that of the shallow conductor. The shallow conductor could involve silicate (basaltic) melt (e.g., Tyburczy and Waff, 1983; Sifré et al., 2014) and conductive components, such as water (e.g., Wang et al., 2006; Yoshino et al., 2009; Pommier et al., 2008) (Figure 7a). Considering that the conductor is located beneath the spreading axis and above the subducted slab, the existence of melt that can be hydrated could explain the low resistivity values of the conductor. We do not consider the influence of CO_2 on the observed resistivity. This is because carbonated melt is expected in deeper part of mantle beneath a spreading ridge than the depth for volatile-free peridotite solidus (e.g., Dasgupta and Hirschmann, 2010), where the melt fraction is very low, and melt fraction becomes higher with decreasing depth and the CO_2 content in melt becomes negligible in the melt production zone shallower than the volatile-free solidus depth. We also note that the amount of CO_2 observed in rock samples and xenoliths in the Marianas is small (Newman et al., 2000; Macpherson et al., 2010) and estimates of some parameters related to the CO_2 content are indistinguishable from those of mid-ocean ridge basalt (Macpherson et al., 2010).

We estimated the melt fraction and water content of the conductor, assuming that the observed resistivity of $10^{0.8}$-$10^{1.4}$ Ω-m represents the bulk resistivity, via modeling with the Hashin-Shtrikman upper bound (HS+) model (Hashin and Shtrikman, 1962). We consider here mixing with two phases by the HS+ model. Assuming that the temperature is 1350-1400°C at depths of 5-20 km, which is a range for a potential temperature of 1350°C with a reasonable adiabatic gradient of 0.3°C/km for the depth range, the melt fraction of dry silicate melt (Tyburczy and Waff, 1983) could be 1-3% (the green box labeled with a circle in Figure 7b) with a dry background mantle of olivine by Gardés et al. (2014). The melt could contain water of up to 1 wt. % (the green box labeled with a circle in Figure 7b), which are less than averages of the water contents at the Mariana back-arc ridge (0.1 wt.%) and the Marianas arc (1 wt.%), respectively (Newman et al., 2000; Kelley et al., 2010); these inclusions of water slightly reduce the melt fraction estimated from the resistivity in inversion model (the green box labeled with a circle in Figure 7b).

The moderately conductive area ($10^{1.2}$-10^2 Ω-m) at ≥20 km depth represents an upwelling zone in the hydrous mantle wedge that could contain melt. The upwelling zone is associated with mantle corner flow and bring a high-temperature material from below (Conder, 2007; Harmon and Blackman, 2010). When we suppose that the temperature is 1200-1400°C for the high-temperature area, the resistivity estimated for the dry olivine mantle (10^2 Ω-m) is higher than the observed resistivity, suggesting that the upwelling zone contains water and partial melt (the green box labeled with a cross in Figure 7a). If olivine in the background mantle contains some amount of water of 0.01-0.18 wt.%, which is maximum water storage capacity at depths of 20-200 km (Hirschmann et al., 2005), laboratory measurements for hydrous olivines predict lower resistivities, which are compatible with the observed resistivity (the green box labeled with a cross in Figure 7a). A small amount of silicate melt, which can contain water, also can exist in the mantle wedge. The melt fraction estimated from the HS+ model for silicate melt with dry background olivine mantle is ≤3% that is compatible with the observed resistivity (the green box labeled with a cross in Figures 7b and 7c). If the background olivine mantle is hydrated, the melt fraction is estimated to be lower than that for the dry background mantle (the green box labeled with a cross in Figure 7c). In any case, the melt fraction estimated never reaches 10% (Figure 7c).

The most significant cause for the shallow flat-shaped conductor and the vertical conductor connected to the shallow body is buoyant upwelling in the mantle wedge, which has the potential to supply melt and water to shallower depths. Such buoyant upwelling can be triggered by dehydration of the subducted slab and melting of the mantle wedge (e.g., Hall and Kincaid, 2001; Gerya and Yuen, 2003; Ikemoto and Iwamori, 2014). The buoyant upwelling material may exist in fluid form, such as melt, water, supercritical fluid, or a mixture (e.g., Cagnioncle et al., 2007; Wilson et al., 2014; Kawamoto et al., 2012; Nielsen and Marschall, 2017). In our inversion models, the root of the buoyant upwelling is located at ~100 km depth at the subducted slab (Figure 5). This depth is coincident with a depth of approximately 80 km where considerable dehydration of the old subducted plate occurs (e.g., van Keken et al., 2011; Kimura and Nakajima, 2014). The conductors in our inversion model suggest that significant dehydration and buoyant mantle upwelling occur in the southern Marianas mantle wedge.

5.2. Asymmetric convection pattern in the mantle wedge

A moderately conductive area at ≥20 km depth shows an asymmetric shape, seen as gradual expansion underlying a resistive area on the remnant arc side (to the left in Figure 5) and a sharp vertical discontinuity contacting a resistive area on the trench side (to the right in Figure 5). This asymmetric conductive area is obviously different from the symmetric triangular conductor that is observed in mid-ocean ridge spreading systems (e.g., Key et al., 2013). The asymmetric area likely delineates a thermal structure and decompression melting area in the mantle wedge. On the former thermal structure, an asymmetric shape is expected for that the distance between the back-arc spreading center and the subducted plate is short and then the mantle flow pattern beneath the spreading center becomes asymmetric under the influence of plate subduction and mantle corner flow (Conder, 2007; Conder et al., 2002; Harmon and Blackman, 2010). On the later decompression melting, the decompression melting area is expected to be broader and deeper than normal mid-ocean ridge system by richer water content in the mantle wedge (Asimow and Langmuir, 2003; Harmon and Blackman, 2010). In the southern Mariana Trough, where an old Pacific plate (~150 Ma; Müller et al., 2008) is subducting and the back-arc spreading center and the subducted slab are close, water from progressive dehydration processes at depths greater than 80 km (e.g., van Keken et al., 2011; Kimura and Nakajima, 2014) could be supplied to the mantle convection or upwelling zones in the mantle wedge. Consequently, melting in the mantle wedge occurs under hydrated conditions, resulting in an increase of total amount of melting and melt retention over a broader zone in mantle in this regime than in a normal mid-ocean ridge system (Asimow and Langmuir, 2003; Harmon and Blackman, 2010). The hydrous mantle wedge, potentially containing melt, is a source of the melt beneath the back-arc spreading ridge at 13°N.

The resistive area overlying the moderately conductive area on the remnant arc side (≤-20 km distance in Figure 5) features residual lithospheric mantle with relatively low temperatures, because this area is far from the upwelling or melt production areas beneath the back-arc spreading center (e.g., Evans et al., 2005; Key et al., 2013). The resistivity of the area, ≥10^2 Ω-m and up to ~10^4 Ω-m, is compatible with dry or slightly hydrated (≤0.01 wt.%) olivine at a temperature of ≤1000°C (Figure 7a), although the actual resistivity of the area could be underestimated due to the lack of MT data on the resistor. The boundary between the upper resistive area and the underlying conductive area reflects the thermal structure of the mantle wedge in this area (Conder, 2007) and also represents the permeability structure for melt transport, which is influenced by the grain size of the mantle material as well as the temperature and rheology (Key et al., 2013; Turner et al., 2015). The gradient of the boundary is approximately 40 km/80 km (vertical depth/horizontal distance) = 1/2 for the 2-D inversion model (Figure 5), which could be larger as approximately 80 km/80 km = 1 as seen in the 3-D inversion model (Figure S11), for the half spreading rate of 33 mm/yr on the western side of our target spreading segment (Seama and Okino, 2015). This gradient may be gentler than that of the EPR segment at 9°30'N, which is 80 km/80 km = 1, with a faster half spreading rate of ~60 mm/yr (Key et al., 2013). This comparison implies that the high-temperature regime possibly extends at shallower depths to the remnant arc side in the mantle wedge beneath the 13°N segment in the slow spreading southern Mariana back-arc system, comparing to the fast spreading mid-ocean ridge system.

The resistive area trenchward of the sharp vertical discontinuity in resistivity (i.e., beyond the second easternmost station, EM10, Figure 5) represents a forearc mantle wedge in low temperature (cold-nose) that contains some fluid interconnected. If the tip of the mantle wedge is decoupled from the convection in the mantle wedge, thus forming the cold-nose structure, consequently the temperature is low (<800°C) (e.g., Wada and Wang, 2009), and the resistivity of the mantle is quite high (10^4 Ω-m or much higher for the low temperature (<800°C) olivine in Figure 8 for mantle). The observed resistivity in this area ($10^{2.5}$-10^3 Ω-m) is lower than the high resistivity expected for the low temperature olivine (Figure 8). A forward modeling test for the high resistivity area in the forearc mantle wedge support that this area is not conductive as $\leq 10^2$ Ω-m, but do not provide constraint on the resistivity value from 3×10^2 Ω-m to 10^4 Ω-m or more. In the test, the resistivity of a rectangular at 60-100 km distance and 10-50 km depth is uniformly changed uniformly from 3×10^1 Ω-m to 10^4 Ω-m or more. The higher resistivity of $\geq 3\times10^2$ Ω-m do not significantly change the total RMS misfit, while 10^2 Ω-m increase the total RMS misfit to 1.30 from 1.14. RMS changes occur mainly at eastern stations (10-40% increase) but also occur at EM4 near the spreading center (30% increase), and those are found mainly at 1920 - 61440 s (10-35% increase). This result suggests that this area may be resistive as $\geq 3\times10^2$ Ω-m but not conductive as $\leq 10^2$ Ω-m. The cold-nose mantle wedge may be serpentinized by fluid that comes from a subducted slab (e.g., Hyndman and Peacock, 2003; Wada and Wang, 2009). The resistivity of serpentinized mantle at the low temperature is so high as similar to that of olivine (Reynard et al., 2011; Guo et al., 2011). Fluid derived from the dehydration process of the slab may exist in the forearc mantle that can be serpentinized. If this fluid formed a network in the forearc mantle wedge, the lowest resistivity of the bulk resistivity for the network in the mantle is 3×10^2 Ω-m or so.

5.3. Implications for the dynamics of the back-arc spreading

We propose that the horizontal distance between the location of the back-arc spreading center and the root of the buoyant upwelling above the subducted slab is a key parameter for the mantle dynamics beneath the back-arc spreading. The result of the small distance in the southern Mariana Trough (~10 km) emerges in our inversion model features of electrical resistivity structure. In the inversion model (Figure 5), the root of the buoyant upwelling is located at ~100 km depth above the subducted slab, which is close to a depth of ~80 km where considerable dehydration of the old subducted plate occurs (e.g., van Keken et al., 2011; Kimura and Nakajima, 2014). The vertical transportation of water and melt from the root by the upwelling entrains surrounding mantle in the wedge to the shallow depth beneath the spreading center, which leads the high melt production at the slow spreading center to produce the fast spreading ridge features in the southern Marianas at 13°N. The small horizontal distance between the spreading center and the root of the buoyant upwelling (Figure 5) is also related to the asymmetrical high-temperature regime in the mantle wedge, which is expected from our inversion model (Figure 5) and is supported by numerical model calculations on mantle convection patterns affected by the proximity of the back-arc spreading center to the subducted slab (Conder, 2007; Harmon and Blackman, 2010).

Our resistivity model in the southern Mariana Trough clearly contrasts with the 2-D electrical resistivity inversion model in the central Mariana Trough at 18°N (Matsuno et al., 2010) (Figure 8). This contrast properly supports our proposal that the horizontal distance between the location of the back-arc spreading center and the root of the buoyant upwelling from the subducted slab is a key parameter for the mantle dynamics beneath the back-arc spreading. Three major different features in resistivity models for two areas well reflect the difference in the key parameter; the spreading center of the southern Marianas locates above the root, while that of the central Marianas locates horizontally 100 km away from the root. The first different model feature in the central Marianas from that in the southern Marianas is a high resistivity area (>3×10^2 Ω-m) beneath the back-arc spreading center down to ~60 km depth. This high resistivity suggests that a melting area is absent (Matsuno et al., 2010) or that the melting area contains only a small amount of silicate melt (<1%) in a 3-D pyramidal shape focused on the spreading center (Matsuno et al., 2012). In contrast to the small amount of melt inferred for the central Mariana Trough (<1%), that for the southern Mariana Trough inferred in this study is greater, approximately 1-3%. The second different model feature is a conductive area (<10^1 Ω-m) beneath the active arc >60 km depth. This low-resistivity zone contains water and melt due to plate subduction and is a source of magmas for arc volcanic activity (Matsuno et al., 2010) by chlorite breakdown (Grove et al., 2009; Manthilake et al., 2016). The difference in resistivities for the zone above the subducted slab at ~60-100 km depths in between the central Marianas (<10^1 Ω-m) and the southern Marianas (~$10^{1.4}$ Ω-m) probably indicates differences in the amount of partial melt and water (or hydrogen) existed in this zone. The smaller amount of melt and water in the southern Marianas than that in the central Marianas suggests that the vertical transportation of melt and water from this deep conductive zone to the shallow depth near the spreading center frequently occur in the southern Marianas to reduce the amount of melt and water in the deep root zone through the buoyant upwelling or the melt segregates from the host rock and migrates upward more effectively in the southern Marianas compared to the central Marianas in which the melt rather ponds. This is probably intensified by the extensional rates in the lithosphere, inferred from GPS data (Kato et al, 2003; Wallace et al., 2005; Wallace et al., 2009), and perhaps the extensional stress in the lithosphere, and the upwelling regime in the upper mantle due to the back-arc spreading. Thirdly, the whole electrical resistivity structures under the spreading centers in two areas are different, one of which is relatively symmetric for the central Marianas and the other of which is asymmetric for the southern Marianas, especially in a wide scale like from -100 km to 100 km distance and at shallower than ~60 km depth (Figures 8a and 8c). All these different features in the resistivity models are satisfactorily explained by the difference in the horizontal distance between the location of the back-arc spreading center and the root of the buoyant upwelling, suggesting that the horizontal distance is a key parameter for the mantle dynamics beneath the back-arc spreading.

Our resistivity model effectively reflects the highly asymmetric seafloor spreading in the southern Mariana Trough, and it well supports a model explaining asymmetric seafloor spreading proposed by Seama and Okino (2015). Those authors concluded that highly asymmetric seafloor spreading is occurring in the southern Mariana Trough because the spreading on the west side of the spreading axis is much faster than that on the east side (trench side), based on the seafloor spreading rates and the seafloor deepening rate. Seama and Okino (2015) also ascribed the asymmetric seafloor spreading to the influence of the low-viscosity region in the mantle wedge due to hydration driven by water released from the subducting slab; the low-viscosity mantle preferentially captures the mantle upwelling zone beneath the spreading axis as the spreading axis has been kept in the area closed to the low-viscosity region in the mantle wedge. Our resistivity model effectively images the vertical conductor beneath the spreading axis in the mantle wedge, and this vertical conductor could correspond to the hydration-induced low-viscosity region in the mantle wedge related to the release of water from the subducting slab. Moreover, the shallow conductor is located beneath the spreading axis but slightly offset toward the trench. This observation indicates that the spreading axis has been kept in the area close to the mantle upwelling zone, which corresponds to the low-viscosity region in the mantle wedge.

The back-arc spreading with the buoyant upwelling from the subducted slab should result in two melt-retained areas (Figure 8), one of which is the shallow conductive area with its most conductive center immediately beneath the PMVC and the other of which is the asymmetric moderately conductive area at deeper depth, probably correspond to origins for rocks sampled at MGR and PMVC. MGR and PMVC rock samples near the MT transect at 13°N are calc-alkaline rocks with various silica-contents from basalt to andesite (Masuda and Fryer, 2015; Brounce et al., 2016). Major and isotope element chemistry of the MGR and PMVC rocks show characteristics of the Mariana Trough lavas farther north including the central Marianas (Masuda and Fryer, 2015; Brounce et al., 2016). Since the MGR and PMVC rocks show geochemical signals found at spreading axes of the Mariana Trough farther north from the 13°N southern Marianas, a source for these rocks is perhaps produced under conditions leading to decompression melt in the mantle wedge of the Mariana Trough. The lava along the spreading axes (<~13.5°N) in the southern Marianas shows more signals of island arc with characteristics of the Mariana Trough basalts in major, trace, and isotope compositions in comparison to those of farther north (>~13.5°N) (Taylor and Martinez, 2003). The mantle source in the southern Mariana Trough is inferred to be more influenced by aqueous fluids and silicate melts from the subducting Pacific plate, comparing to the central Mariana area (Pearce et al., 2005). The shallow conductive area with its most conductive center immediately beneath the PMVC probably represents a reservoir of melts for MGR and PMVC rocks. Our inversion model suggests that the melts were formed immediately above the subducted slab and were transported by mantle upwelling. The asymmetric moderately conductive area at deeper depth probably represents a melt source for MGR rocks. Our inversion model suggest that this melt source is generated in the decompression melting area in the mantle wedge. FNVC samples are tholeiitic and possess Mariana-arc features (Masuda and Fryer, 2015; Brounce et al., 2016). Melt in the shallow conductive area might be a source for FNVC rocks, but it should be cautious to relate the geochemical signature of the FNVC rocks to the electrical resistivity model because the FNVC was formed before the rifting of the SEMFR has started at 2.7-3.7 Ma (Ribeiro et al., 2013; Masuda and Fryer, 2015).

6. Summary

Our electrical resistivity structure at the 13°N back-arc spreading segment in the southern Mariana Trough showed characteristic features (Figure 8), which are a conductive area beneath the back-arc spreading center with a possible slight trenchward offset, a moderately conductive and asymmetric area expanding under the spreading center, a resistive area thickening away from the spreading center toward the remnant arc side, and a broad resistive area on the trench side. The model structures are closely related to the distribution and the amount of melt and water (or hydrogen) and thermal structure, and reveal the melting process beneath the back-arc spreading center and the dehydration processes related to the subduction of the Pacific plate in the upper mantle in the southern Mariana Trough (Figure 8). Our electrical resistivity model effectively images the vertical conductor in the mantle wedge whose shallow part is located beneath the spreading axis but slightly offset toward the trench, suggesting that the spreading axis has been kept in the area close to the mantle upwelling zone as the model explaining the highly asymmetric seafloor spreading proposed by Seama and Okino (2015). Moreover, our electrical resistivity model in the southern Mariana Trough clearly differs from the structure in the central Mariana Trough at 18°N, which lacks a conductor beneath the ridge center. The model difference between these two regions in the Mariana Trough shows the clearly different distributions of melt and water (or hydrogen). On the basis of the difference, we propose that the horizontal distance between the location of the back-arc spreading center and the root of the buoyant upwelling at ~100 km depth of the subducted slab is a key parameter for the mantle dynamics beneath the back-arc spreading.

Acknowledgments

We greatly thank the captain (Satoshi Susami), officers, crews, and scientific party members (Maho Kimura, Yuki Shibata, Shingo Kato, Hiroko Makita, Takehi Isse, Satoshi Okada, Masayuki Toizumi, Morifumi Takaesu, and Hisanori Iwamoto) for successfully completing the marine MT experiment during YK10-10 and YK10-15 cruises of JAMSTEC *S/V Yokosuka*. We conducted this work under the support by the scientific program of TAIGA (Trans-crustal Advection and In-situ reaction of Global sub-seafloor Aquifer, #20109002) and JSPS Grant-in-Aid (15H03717) sponsored by the Ministry of Education, Culture, Sports, Science and Technology (MEXT) of Japan. Alan D. Chave and Rob. L. Evans let us use the 2-D anisotropic inversion program, and Yoshiya Usui let us use the 3-D inversion program and associated pre- and post-processing tools. We thank Tomoeki Nakakuki for fruitful discussions. TM thanks Hisashi Utada and Kiyoshi Baba for comments on this work. Stephen A. Bowden and Mari Hamahashi kindly edit English in some portions of the manuscript. Comments by two anonymous reviewers and Associate Editor, Max Moorkamp, after their careful and thorough reading of the manuscript were valuable and constructive to improve the manuscript. All the figures were produced with Generic Mapping Tool, GMT [Wessel et al., 2013]. Data of the MT responses observed are available in data catalog of JAMSTEC, http://www.godac.jamstec.go.jp/catalog/data_catalog/index_en.html, or at the following link on the figshare site, https://figshare.com/articles/dataset/YK10-10_YK10-15_MTresp_tar/14572053.

References

Amante, C., and .B. W., Eakins (2009). ETOPO1 1 arc-minute global relief model: procedures, data sources and analysis. In: NOAA Technical Memorandum NESDIS NGDC-24, p. 19.

Asimow, P. D., and Langmuir, C. H. (2003). The importance of water to oceanic mantle melting regimes. *Nature*, 421, 815-820. https://doi.org/10.1038/nature01429

Baba, K., and Seama, N. (2002). A new technique for the incorporation of seafloor topography in electromagnetic modeling. *Geophys. J. Int.*, 150, 392-402. https://doi.org/10.1046/j.1365-246X.2002.01673.x

Baba, K., and A. D. Chave (2005), Correction of seafloor magnetotelluric data for topographic effects during inversion, *J. Geophys. Res.*, 110, B12105, doi:10.1029/2004JB003463

Baba, K., Chave, A. D., Evans, R. L., Hirth, G., and Mackie, R. L. (2006). Mantle dynamics beneath the East Pacific Rise at 17°S: Insights from the Mantle Electromagnetic and Tomography (MELT) experiment. *J. Geophys. Res.*, 111, B02101. https://doi.org/10.1029/2004JB003598

Becker, N., Fryer, C., P., and Moore, G. F. (2010). Malaguan-Gadao Ridge: Identification and implications of a magma chamber reflector in the southern Mariana Trough. *Geochem. Geophys. Geosyst.*, 11, Q04X13. https://doi.org/10.1029/2009GC002719

Bird, P. (2003). An updated digital model of plate boundaries. *Geochem. Geophys. Geosyst.*, 4(3), 1027. https://doi.org/10.1029/2001GC000252

Brounce, M., Kelley, K. A., Stern, R., Martinez, F., and Cottrell, E. (2016). The Fina Nagu volcanic complex: Unusual submarine arc volcanism in the rapidly deforming southern Mariana margin. *Geochem. Geophys. Geosyst.*, 17, 4078-4091. https://doi.org/10.1002/2016GC006457

Cagnioncle, A.-M., Parmentier, E. M., and Elkins-Tanton, L. T. (2007). Effect of solid flow above a subducting slab on water distribution and melting at convergent plate boundaries. *J. Geophys. Res.*, 112, B09402. https://doi.org/10.1029/2007JB004934

Chave, A. D., and Thomson, D. J. (2004). Bounded influence estimation of magnetotelluric response functions. *Geophys. J. Int.*, 157, 988–1006. https://doi.org/10.1111/j.1365-246X.2004.02203.x

Conder, J. A. (2007). Temperature structure of the Mariana system from geodynamical modeling. Joint NSF-MARGINS and IFREE Workshop: Subduction Factory Studies in the Izu-Bonin-Mariana Arc System: Results and Future Plans, Honolulu, Hawaii, (Available at http://www.nsf-margins.org/IBM07/index.html).

Conder, J. A., Wiens, D. A., and Morris, J. (2002). On the decompression melting structure at volcanic arcs and back-arc spreading centers. *Geophys. Res. Lett.*, 29(15), https://doi.org/10.1029/2002GL015390

Constable, S., Shankland, T. J., and Duba, A. (1992). The electrical conductivity of an isotropic olivine mantle. *J. Geophys. Res.*, 97(B3), 3397-3404. https://doi.org/10.1029/91JB02453

Constable, S. (2006). SEO3: A new model of olivine electrical conductivity. *Geophys. J. Int.*, 166, 435-437. https://doi.org/10.1111/j.1365-246X.2006.03041.x

Dalton, C. A, Langmuir, C. H., Gale, A. (2014). Geophysical and geochemical evidence for deep temperature variations beneath mid-ocean ridges. *Science*, 344(6179), 80-83. https://doi.org/10.1126/science.1249466

Dasgupta, R., and Hirschmann, M. M. (2010). The deep carbon cycle and melting in Earth's interior. *Earth Planet. Sci. Lett.*, 298(1-2), 1-13. https://doi.org/10.1016/j.epsl.2010.06.039

Dunn, R. A., and Martinez, F. (2011). Contrasting crustal production and rapid mantle transitions beneath back-arc ridges. *Nature*, 469, 198-202. https://doi.org/10.1038/nature09690

England, P. C., and Katz, R. F. (2010). Melting above the anhydrous solidus controls the location of volcanic arcs. *Nature*, 467, 700-703. https://doi.org/10.1038/nature09417

Evans, R. L., Hirth, G., Baba, K., Forsyth, D., Chave, A., and Mackie, R. (2005). Geophysical evidence from the MELT area for compositional controls on oceanic plates. *Nature*, 437, 249-252. https://doi.org/10.1038/nature04014

Evans, R. L., Wannamaker, P. E., McGary, R. S., Elsenbeck, J. (2013). Electrical structure of the central Cascadia subduction zone: The EMSLAB Lincoln Line revisited. *Earth Planet. Sci. Lett.*, 402, 265-274. https://doi.org/10.1016/j.epsl.2013.04.021

Forsyth, D. W. (1992). Geophysical constraints on mantle flow and melt generation beneath mid-ocean ridges. In J. P. Morgan, D. K. Blackman, J. M. Sinton (Eds.), *Mantle flow and melt generation at mid-ocean ridges, Geophysical Monograph Series* (Vol. 71, pp. 183-280). Washington, DC: American Geophysical Union. Htttps://doi.org/10.1029/GM071p0001

Gardés, E., Gaillard, F., and Tarits, P. (2014), Toward a unified hydrous olivine electrical conductivity law. *Geochem. Geophys. Geosyst.*, 15, 4984-5000. https://doi.org/10.1002/2014GC005496

Gerya, T. V., and Yuen, D. A. (2003). Rayleigh-Taylor instabilities from hydration and melting propel ‘cold plumes’ at subduction zones. *Earth Planet. Sci. Lett.*, 212, 47-62. https://doi.org/10.1016/S0012-821X(03)00265-6

Grove, T. L., Till, C. B., Lev, E., Chatterjee, N., and Médard, E. (2009). Kinematic variables and water transport control the formation and location of arc volcanoes. *Nature*, 459, 694-697. https://doi.org/10.1038/nature08044

Guo, X., Yoshino, T., and Katayama, I. (2011). Electrical conductivity anisotropy of deformed talc rocks and serpentinites at 3 GPa. *Phys. Earth Planet. Inter.*, 188, 69-81. https://doi.org/10.1016/j.pepi.2011.06.012

Hayes, G. P., Wald, D. J., and Johnson, R. L. (2012). Slab1.0: A three-dimensional model of global subduction zone geometries. *J. Geophys. Res.*, 117, B01302. https://doi.org/10.1029/2011JB008524

Hacker, B. R., Abers, G. A., and Peacock, S. M. (2003). Subduction factory, 1, Theoretical mineralogy, densities, seismic wave speeds, and H_2O contents. *J. Geophys. Res.*, 108(B1), 2029. https://doi.org/10.1029/2001JB001127

Hall, P. S., and Kincaid, C. (2001). Diapiric flow at subduction zones: A recipe for rapid transport. *Science*, 292(5526), 2472-2475. https://doi.org/10.1126/science.1060488

Harmon, N., and Blackman, D. K. (2010). Effects of plate boundary geometry and kinematics on mantle melting beneath the back-arc spreading centers along the Lau Basin. *Earth Planet. Sci. Lett.*, 298, 334-346. https://doi.org/10.1016/j.epsl.2010.08.004

Hashin, Z., and Shtrikman, S. (1962). A variational approach to the theory of the effective magnetic permeability of multiphase materials, *J. Appl. Phys.*, 33, 3125-3131. https://doi.org/10.1063/1.1728579

Hirschmann, M. M., Aubaud, C., and Withers, A. C. (2005). Storage capacity of H_2O in nominally anhydrous minerals in the upper mantle. *Earth Planet. Sci. Lett.*, 236, 167-181. https://doi.org/10.1016/j.epsl.2005.04.022

Hyndman, R. D., and Peacock, S. M. (2003). Serpentinization of the forearc mantle. *Earth Planet. Sci. Lett.*, 212, 417-432. https://doi.org/10.1016/S0012-821X(03)00263-2.

Ikemoto, A., and H. Iwamori (2014). Numerical modeling of trace element transportation in subduction zones: implications for geofluid processes. *Earth Planets Space*, 66:26, https://doi.org/10.1186/1880-5981-66-26

Ito, G., Lin, J., and Graham, D. (2003). Observational and theoretical studies of the dynamics of mantle plume–mid-ocean ridge interaction. *Rev. Geophys.*, 41, 4, 1017, https://doi:10.1029/2002RG000117

Kato, T., Beavan, J., Matsushima, T., Kotake, Y., Camacho, J. T., and Nakao, S. (2003). Geodetic evidence of back-arc spreading in the Mariana Trough. *Geophys. Res. Lett.*, 30(12), 1625. https://doi.org/10.1029/2002GL016757

Kawamoto, T., Kanzaki, M., Mibe, K., Matsukage, K. N., and Ono, S. (2012). Separation of supercritical slab-fluids to form aqueous fluid and melt components in subduction zone magmatism. *Proc Natl Acad Sci USA.*, 109(46), 18695-18700. https://doi.org/10.1073/pnas.1207687109

Key, K., Constable, S. Liu, L., and Pommier, A. (2013), Electrical image of passive mantle upwelling beneath the northern East Pacific Rise, *Nature*, 495, 499-502. https://doi.org/0.1038/nature11932

Kelley, K. A., Plank, T., Grove, T. L., Stolper, E. M., Newman, S., and Hauri, E. (2006). Mantle melting as a function of water content beneath back-arc basins. *J. Geophys. Res.*, 111, B09208. https://doi.org/10.1029/2005JB003732

Kelley, K. A., Plank, T., Newman, S., Stolper, E. M., Grove, T. L., Parman, S., Hauri, E. H. (2010). Mantle melting as a function of water content beneath the Mariana Arc, *J. Petrol.*, 51(8), 1711-1738. https://doi.org/10.1093/petrology/egq036

Kimura, J.-I., and Nakajima, J. (2014). Behaviour of subducted water and its role in magma genesis in the NE Japan arc: A combined geophysical and geochemical approach. *Geochim. Cosmochim. Acta*, 143, 165-188. https://doi.org/10.1016/j.gca.2014.04.019

Kitada, K., Seama, N., Yamazaki, T., Nogi, Y., and Suyehiro, K. (2006). Distinct regional differences in crustal thickness along the axis of the Mariana Trough, inferred from gravity anomalies. *Geochem. Geophys. Geosyst.*, 7, Q04011. https://doi.org/10.1029/2005GC001119

Ledo, J., Gueralt, P., Marti, A., and Jones, A. G. (2002). Two-dimensional interpretation of three-dimensional magnetotelluric data: an example of limitations and resolution. *Geophys. J. Int.*, 150, 127-139. https://doi.org/10.1046/j.1365-246X.2002.01705.x

Lin, J., and Morgan, J. P. (1992). The spreading rate dependence of three-dimensional mid-ocean ridge gravity structure, *Geophys. Res. Lett.*, 19(1), 13-16. https://doi.org/10.1029/91GL03041

Liu, C.-Z., Snow, J. E., Hellebrand, E., Brügmann, G., von der Handt, A., Büchl, A. and Hofmann, A. W. (2008). Ancient, highly heterogeneous mantle beneath Gakkel ridge, Arctic Ocean, *Nature*, 452, 311-316. https://doi.org/10.1038/nature06688

Macdonald, K. C., Scheirer, D. S., and Carbotte, S. M. (1991). Mid-ocean ridges: Discontinuities, segments and giant cracks, *Science*, 253(5023), 986-994.

https://doi.org/10.1126/science.253.5023.986

Macpherson, C. G., Hilton, D. R., and Hammerschmidt, K. (2010). No slab-derived CO_2 in Mariana Trough back-arc basalts: Implications for carbon subduction and for temporary storage of CO_2 beneath slow spreading ridges. *Geochem. Geophys. Geosyst.*, 11, Q11007. https://doi.org/10.1029/2010GC003293

Manthilake, G., Bolfan-Casanova, N., Novella, D., Mookherjee, M., and Andrault, D. (2016). Dehydration of chlorite explains anomalously high electrical conductivity in the mantle wedges. *Science Advances*, 2(5), e1501631. https://doi.org/10.1126/sciadv.1501631

Martínez, F., Fryer, P., and Becker, N. (2000). Geophysical characteristics of the southern Mariana Trough, 11°50′N-13°40′N. *J. Geophys. Res.*, 105(B7), 16591-16607. https://doi.org/10.1029/2000JB900117

Martinez, F., and Taylor, B. (2002). Mantle wedge control on back-arc crustal accretion, *Nature*, 416, 417-420. https://doi.org/10.1038/416417a

Masuda, H., and Fryer, P. (2015). Geochemical characteristics of active backarc basin volcanism at the southern end of the Mariana Trough. In J. Ishibashi et al. (Eds.), *Subseafloor Biosphere Linked to Global Hydrothermal Systems; TAIGA Concept* (pp. 241-251). Tokyo: Springer Japan. https://doi.org/10.1007/978-4-431-54865-2_21

Matsuno, T., Seama, N., and Baba, K. (2007). A study on correction equations for the effect of seafloor topography on ocean bottom magnetotelluric data. *Earth Planets Space*, 59, 981-986. https://doi.org/10.1016/j.pepi.2007.02.014

Matsuno, T., Seama, N., Evans, R. L., Chave, A. D., Baba, K., White, A., Goto, T., Heinson, G., Boren, G., Yoneda, A., and Utada, H. (2010). Upper mantle electrical resistivity structure beneath the central Mariana subduction system. *Geochem. Geophys. Geosyst.*, 11, Q09003. https://doi.org/10.1029/2010GC003101

Matsuno, T., Evans, R. L., Seama, N., and Chave, A. D. (2012). Electromagnetic constraints on a melt region beneath the central Mariana back-arc spreading ridge. *Geochem. Geophys. Geosyst.*, 13, Q10017. https://doi.org/10.1029/2012GC004326

Matsuno, T., Chave, A. D., Jones, A. G., Muller, M. R., and Evans, R. L. (2014). Robust magnetotelluric inversion. *Geophys. J. Int.*, 196, 1365-1374. https://doi.org/10.1093/gji/ggt484

McGary, R. S., Evans, R. L., Wannamaker, P. E., Elsenbeck, J., and Rondenay, S. (2014). Pathway from subducting slab to surface for melt and fluids beneath Mount Rainier. *Nature*, 511, 338-340. https://doi.org/10.1038/nature13493

Miller, M. S., Kennett, B. L. N., and Toy, V. G. (2006). Spatial and temporal evolution of the subducting Pacific plate structure along the western Pacific margin. *J. Geophys. Res.*, 111, B02401. https://doi.org/10.1029/2005JB003705

Müller, R. D., M. Sdrolias, C. Gaina, and W. R. Roest (2008), Age, spreading rates, and spreading asymmetry of the world's ocean crust, *Geochem. Geophys. Geosyst.*, 9, Q04006. doi:10.1029/2007GC001743

Newman, S., Stolper, E., and Stern, R. (2000). H_2O and CO_2 in magmas from the Mariana arc and back arc systems. *Geochem. Geophys. Geosyst.*, 1(5), 1013. https://doi.org/10.1029/1999GC000027

Nielsen, S. G., and Marschall, H. R. (2017). Geochemical evidence for mélange melting in global arcs. *Science Advances*, 3(4), e1602402. https://doi.org/10.1126/sciadv.1602402

Nolasco, R., Tarits, P., Filloux, J. H., and Chave, A. D. (1998). Magnetotelluric imaging of the Society Islands hotspot. *J. Geophys. Res.*, 103(B12), 30287-30309

Pearce J. A., Stern, R. J., Bloomer, S. H., and Fryer, P. (2005). Geochemical mapping of the Mariana arc-basin system: Implications for the nature and distribution of subduction components. *Geochem. Geophys. Geosyst.*, 6, Q07006. https://doi.org/10.1029/2004GC000895

Pommier, A., Gaillard, F., Pichavant, M., and Scaillet, B. (2008). Laboratory measurements of electrical conductivities of hydrous and dry Mount Vesuvius melts under pressure. *J. Geophys. Res.*, 113, B05205. https://doi.org/10.1029/2007JB005269

Reynard, B., Mibe, K., and Van de Moortèleet, B. (2011). Electrical conductivity of the serpentinised mantle and fluid flow in subduction zones. *Earth Planet. Sci. Lett.*, 307, 387-394. https://doi.org/10.1016/j.epsl.2011.05.013

Ribeiro, J. M., Stern, R. J., Kelley, K. A., Martinez, F., Ishizuka, O., Manton, W. I., and Ohara, Y. (2013). Nature and distribution of slab-derived fluids and mantle sources beneath the Southeast Mariana forearc rift. *Geochem. Geophys. Geosyst.*, 14. https://doiorg/10.1002/ggge.20244

Rodi, W., and Mackie, R. L. (2001). Nonlinear conjugate gradients algorithm for 2-D magnetotelluric inversion. *Geophysics*, 66, 174-187. https://doi.org/10.1190/1.1444893

Sato, T., Mizuno, M., Takata, H., Yamada, T., Isse, T., Mochizuki, K., Shinohara, M., and Seama, N. (2015). Seismic structure and seismicity in the southern Mariana Trough and their relation to hydrothermal activity. In J. Ishibashi et al. (Eds.), *Subseafloor Biosphere Linked to Global Hydrothermal Systems; TAIGA Concept* (pp. 241-251). Tokyo: Springer Japan. https://doi.org/10.1007/978-4-431-54865-2_18

Schmidt, M. W., and Poli, S. (1998). Experimentally based water budgets for dehydrating slabs and consequences for arc magma generation. *Earth Planet. Sci. Lett.*, 163, 361-379. https://doi.org/10.1016/S0012-821X(98)00142-3

Sdrolias, M., and Müller, R. D. (2006). Controls on back-arc basin formation, *Geochem. Geophys. Geosyst.*, 7, Q04016. https://doi.org/10.1029/2005GC001090

Seama, N., and Okino, K. (2015). Asymmetric seafloor spreading of the southern Mariana Trough back-arc basin. In J. Ishibashi et al. (Eds.), *Subseafloor Biosphere Linked to Global Hydrothermal Systems; TAIGA Concept* (pp. 241-251). Tokyo: Springer Japan. https://doi.org/10.1007/978-4-431-54865-2_20

Seama, N., Sato, H., Nogi, Y., and Okino, K. (2015). The mantle dynamics, the crustal formation, and the hydrothermal activity of the southern Mariana Trough back-arc basin. In J. Ishibashi et al. (Eds.), *Subseafloor Biosphere Linked to Global Hydrothermal Systems; TAIGA Concept* (pp. 241-251). Tokyo: Springer Japan. https://doi.org/10.1007/978-4-431-54865-2_17

Shimizu, H., Yoneda, A., Baba, K., Utada, H., and Palshin, N. A. (2011). *Sq* effect on the electromagnetic response functions in the period range between 10^4 and 10^5 s. *Geophys. J. Int.*, 186(1), 193-206. https://doi.org/10.1111/j.1365-246X.2011.05036.x

Sifré, D., Gardés, E., Massuyeau, M., Hashim, L., Hier-Majumder, S., and Gaillard, F. (2014). Electrical conductivity during incipient melting in the oceanic low-velocity zone. *Nature*, 509, 81-85. https://doi.org/10.1038/nature13245

Stern, R. J., Tamura, Y., Masuda, H., Fryer, P., Martinez, F., Ishizuka, O. and Bloomer, S. H. (2013). How the Mariana Volcanic Arc ends in the south. *Island Arc*, 22, 133-148. https://doi.org/10.1111/iar.12008

Tatsumi, Y. (1986). Formation of the volcanic front in subduction zones. *Geophys. Res. Lett.*, 13(8), 717-720. https://doi.org/ 10.1029/GL013i008p00717

Taylor, B., Martinez, F. (2003). Back-arc basin basalt systematics, *Earth Planet. Sci. Lett.*, 210, 481-497. https://doi.org/10.1016/S0012-821X(03)00167-5

Thebault, E. et al. (2015). International Geomagnetic Reference Field: the 12th generation. *Earth Planets Space*, 67:79. https://doi.org/10.1186/s40623-015-0228-9

Tyburczy, J. A., and Waff, H. S. (1983). Electrical conductivity of molten basalt and andesite to 25 kilobars pressure: Geophysical significance and implications for charge transport and melt structure, *J. Geophys. Res.*, 88(B3), 2413-2430. https://doi.org/10.1029/JB088iB03p02413

Turner, A. J., Katz, R. F., and Behn, M. D. (2015). Grain-size dynamics beneath mid-ocean ridges: Implications for permeability and melt extraction, *Geochem. Geophys. Geosyst.*, 16, 925-946. https://doi.org/10.1002/2014GC005692

Usui, Y. (2015). 3-D inversion of magnetotelluric data using unstructured tetrahedral elements: applicability to data affected by topography. *Geophys. J. Int.*, 202(2): 828-849. https://doi.org/10.1093/gji/ggv186

Usui, Y., T. Kasaya, Y. Ogawa, and H. Iwamoto (2018). Marine magnetotelluric inversion with an unstructured tetrahedral mesh. *Geophys. J. Int.*, 214(2): 952-974. https://doi.org/10.1093/gji/ggy171

van Keken, P. E., Hacker, B. R., Syracuse, E. M., and Abers, G. A. (2011). Subduction factory: 4. Depth-dependent flux of H_2O from subducting slabs worldwide. *J. Geophys. Res.*, 116, B01401. https://doi.org/10.1029/2010JB007922

Wada, I., and Wang, K. (2009). Common depth of slab-mantle decoupling: Reconciling diversity and uniformity of subduction zones. *Geochem. Geophys. Geosyst.*, 10, Q10009. https://doi.org/10.1029/2009GC002570

Wada, I., and Behn, M. D. (2015). Focusing of upward fluid migration beneath volcanic arcs: Effect of mineral grain size variation in the mantle wedge. *Geochem. Geophys. Geosyst.*, 16, 3905-3923. https://doi.org/10.1002/2015GC005950

Wallace, L. M., R. McCaffrey, J. Beavan, and S. Ellis (2005). Rapid microplate rotations and back-arc rifting at the transition between collision and subduction, *Geology*, 33, 857-860. doi:10.1130/G21834.1

Wallace, L. M., S. Ellis, and P. Mann (2009). Collisional model for rapid fore-arc block rotations, arc curvature, and episodic back-arc rifting in subduction settings, *Geochem. Geophys. Geosyst.*, 10, Q05001. doi:10.1029/2008GC002220

Wang, D., Mookherjee, M., Xu, Y., and Karato, S. (2006). The effect of water on the electrical conductivity of olivine. *Nature*, 443, 977-980. https://doi.org/10.1038/nature05256

Wannamaker, P. E., Hohmann, G. W., and Ward, S. H. (1984). Magnetotelluric responses of three-dimensional bodies in layered earths. *Geophysics*, 49, 1517-1533

Wessel, P., Smith, W. H. F., Scharroo, R., Luis, J., and Wobbe, F. (2013). Generic Mapping Tools: Improved version released. Eos, trans. AGU, 94(45), 409-420. https://doi.org/10.1002/2013EO450001

Wiens, D. A., Kelley, K. A., and Plank, T. (2006). Mantle temperature variations beneath back-arc spreading center inferred from seismology, petrology, and bathymetry. *Earth Planet. Sci. Lett*., 248, 30-42. https://doi.org/10.1016/j.epsl.2006.04.011

Wilson, C. R., Spiegelman, M., van Keken, P. E., and Hacker, B. R. (2014). Fluid flow in subduction zones: The role of solid rheology and compaction pressure. *Earth Planet. Sci. Lett*., 401, 261-274. https://doi.org/10.1016/j.epsl.2014.05.052

Yoshino, T., Matsuzaki, T., Shatskiy, A., and Katsura, T. (2009), The effect of water on the electrical conductivity of olivine aggregates and its implications for the electrical structure of the upper mantle. *Earth Planet. Sci. Lett.*, 288, 291-300. https://doi.org/10.1016/j.epsl.2009.09.032

Table

Station ID	Latitude (N)	Longitude (E)	Water Depth [m]	E-field	Remote B-field
EM1	13°19.25’	143°02.80’	3924	Available	EM6
EM2	13°10.92’	143°15.09’	3749	Available	EM10
EM3	13°06.69’	143°21.56’	3567	Available	EM7
EM4	13°02.37’	143°28.05’	3255	+	+
EM5	12°58.00’	143°34.53’	3086	EM8	N/A
EM6	12°56.74’	143°36.41’	2868	Available	EM5
EM7	12°55.43’	143°38.18’	3123	Available	EM5
EM8	12°53.47’	143°41.21’	3316	Available	EM5
EM9	12°49.13’	143°47.57’	2569	++	++
EM10	12°45.09’	143°53.96’	3685	Available	N/A
EM11	12°40.82’	144°00.47’	3751	EM10	EM6

Table 1

Station information. Station ID is numbered from the northwesternmost station to the southeasternmost one; see also Figure 1. Latitude and longitude is the location of the ship at the time of deployment of the instrument, and water depth is derived from the multi-narrow beam bathymetric data (Kitada et al., 2006). The symbol “+” for EM4 means that EM field data were obtained by the experiment, but the MT response estimated from the data had a low squared coherency between the electric field observed and that predicted from the MT response estimated and the magnetic field observed, and were not used in the inversion. The symbol “++” for EM9 means that this instrument has not yet been recovered.

Figures

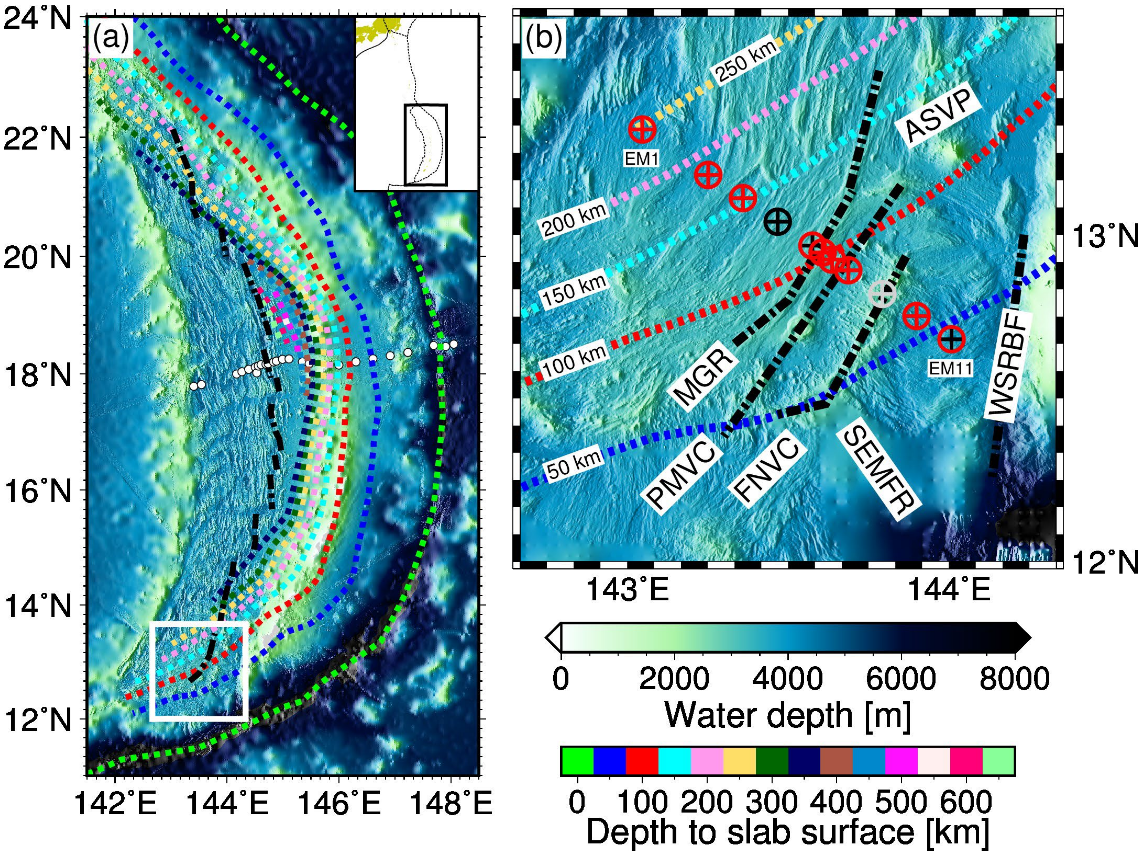

Figure 1

(a) Bathymetric map, which derives from multi-narrow beam data (Kitada et al., 2006) and the ETOPO1 data (Amante and Eakins, 2009), with depth contours of the surface of the subducted Pacific slab (colored dotted lines; Hayes et al., 2012) and the location of the Mariana Trench (light green dotted line; Bird, 2003), as well as ridge centers of the back-arc spreading in the Mariana Trough (black dash-dotted line; Kitada et al., 2006). The white box represents the range of the map in Figure 1b, and the range of this map is shown by the black rectangle in the right-top inset showing the plate boundaries (Bird, 2003). White dots at around 18°N indicate MT stations used for obtaining an electrical resistivity structure in the central Marianas (Matsuno et al., 2010).

(b) Bathymetric map with marine MT observational stations (symbols). Circles and crosses indicate locations of magnetic field data and electric field data, respectively. The colors red, black, and gray for the symbols indicate stations from which the data were used in the inversion, stations from which data were obtained but not used in inversion, and stations at which the instrument was not recovered, respectively. The station names are numbered from northwest to southeast (the northwesternmost station is called EM1, and the southeasternmost one is called EM11); see also Table 1. The abbreviations in this map are as follows: MGR: Malaguana-Gadau Ridge, PMVC: Patgon-Masala Volcanic Chain, FNVC: Fina Nagu Volcanic Chain, ASVP: Alphabet Seamount Volcano Province, WSRBF: West Santa Rosa Bank Fault, SEMFR: Southeast Mariana Forearc Rift (Stern et al., 2013; Masuda and Fryer, 2015).

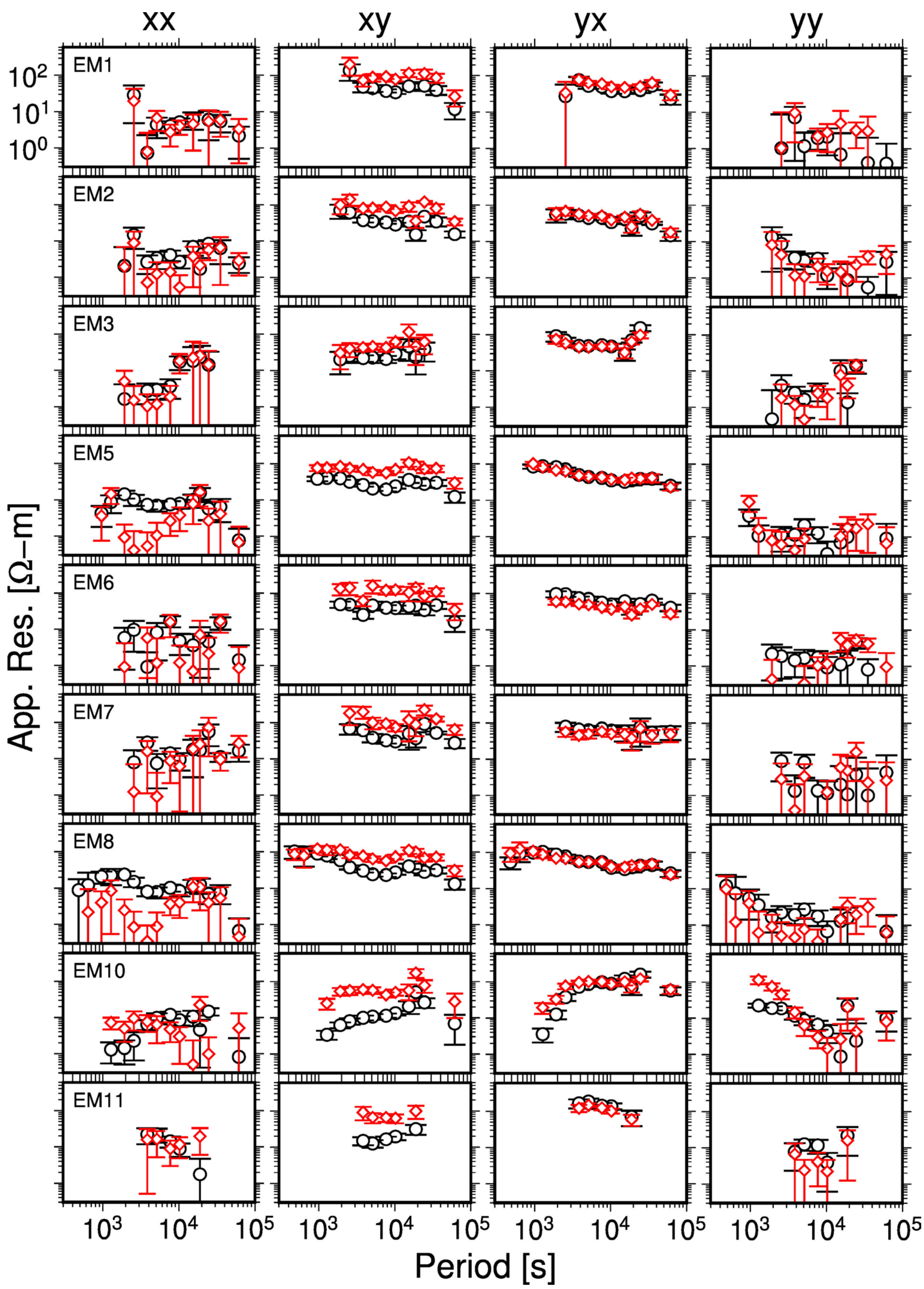

Figure 2

Apparent resistivities for all four elements and all stations before and after the correction of topographic distortions (black circle and red diamond, respectively). Error bars show one standard error of the observations. An annotation for the vertical axis is shown only in the upper-left-most panel but is common to all the other panels. The station names are shown in the upper-left corner in the leftmost panels.

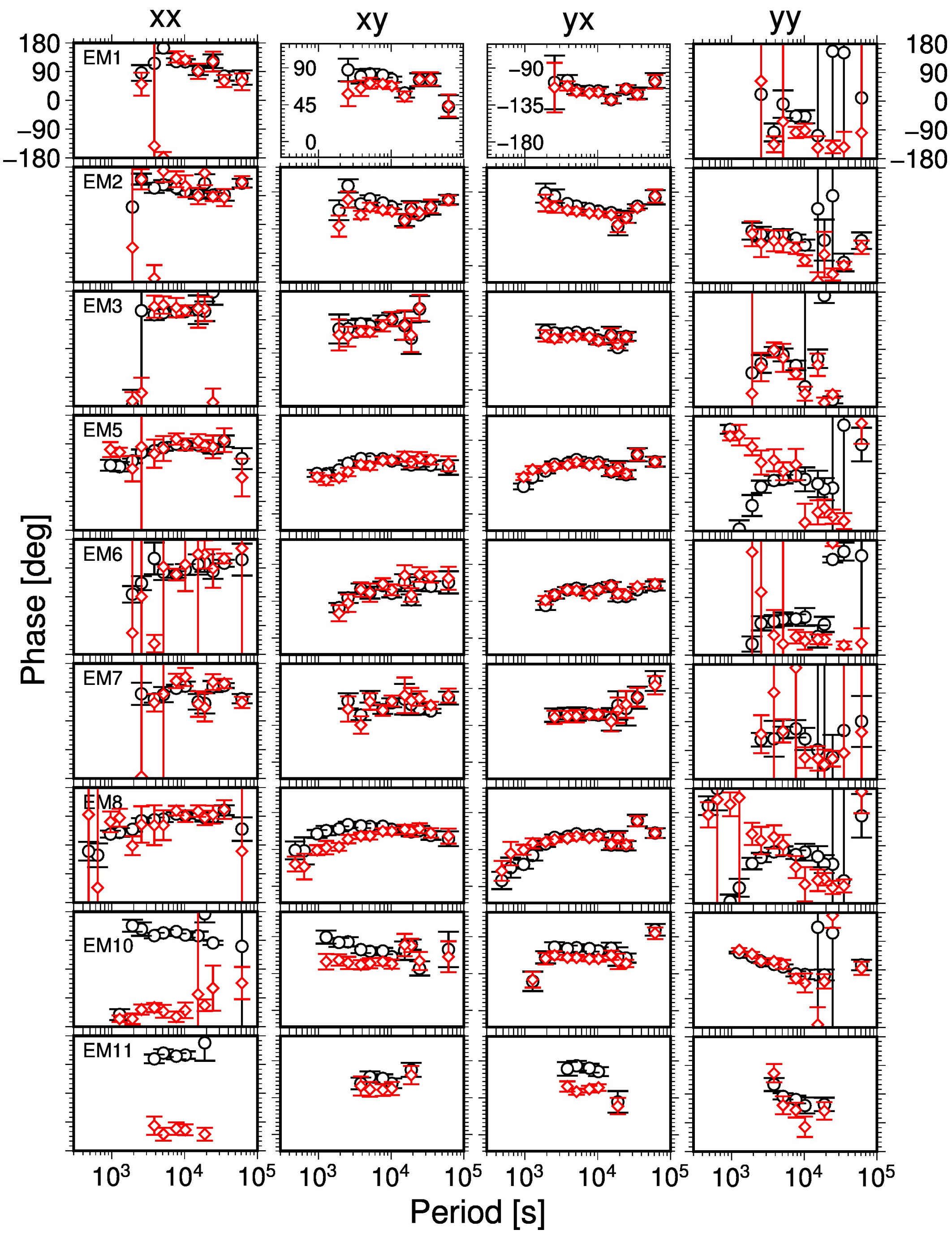

Figure 3

Phase values for all four elements and all stations before and after the correction of topographic distortions. The symbols and the error bars are the same as in Figure 2. Note that ranges of the phase values for off-diagonal elements and diagonal elements are different. Annotations for the vertical axis are shown only in the top panels but are common to each MT impedance element panel. The station names are shown in the upper-left corner in the leftmost panels.

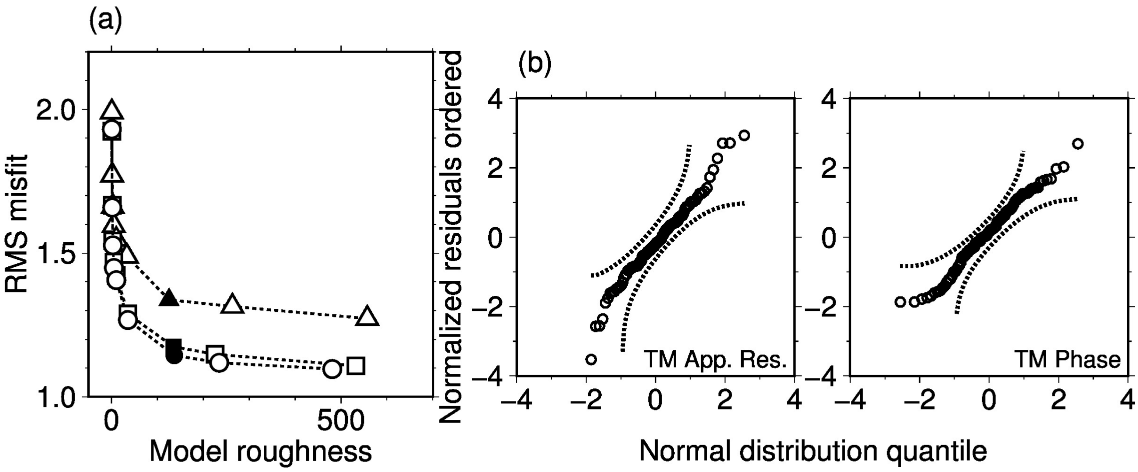

Figure 4

(a) RMS misfits and model roughness values for 2-D electrical resistivity models in the robust inversion processing. The model constraint in the inversion is only model smoothness. The robust inversion processing was applied two times, and the resulting values are shown by triangles, squares, and circles for the 0th, 1st, and 2nd robust inversion runs. At each run, 9 values for the regularization parameter of model smoothness (τ_s) were used: 300, 100, 30, 10, 3, 1, 0.3, 0.1, and 0.03. The optimal value of the regularization parameter is 0.3 for all robust runs, as shown by the filled symbols.

(b) Quantile-quantile plot with 95% confidence limits for the results of the final inversion (the 2nd run).

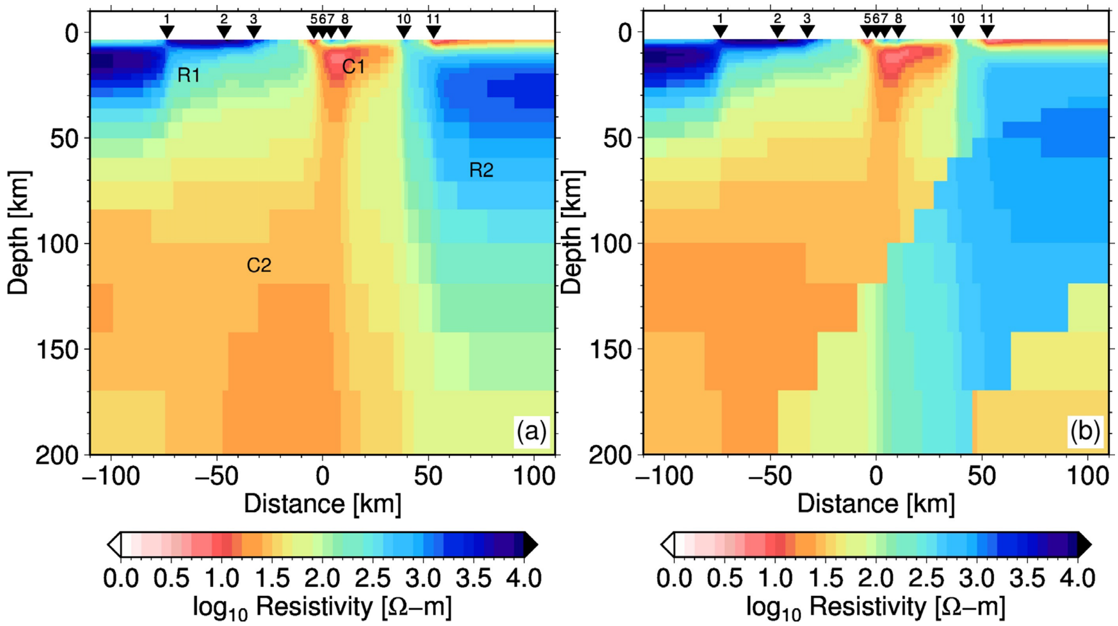

Figure 5

Optimal 2-D electrical resistivity inversion models (a) with constraints on only model smoothness and (b) with constraints on model smoothness and allowance for resistivity jumps surrounding the subducted Pacific slab. The tip of the subducted slab, which was taken into account for the resistivity jump in Figure 5b, terminates at 200 km depth. Stations are represented by inverted triangles with numbers near the top of each figure. Note that the seafloor spreading center is located at 0 km distance, and that the station located at the spreading center is EM6.

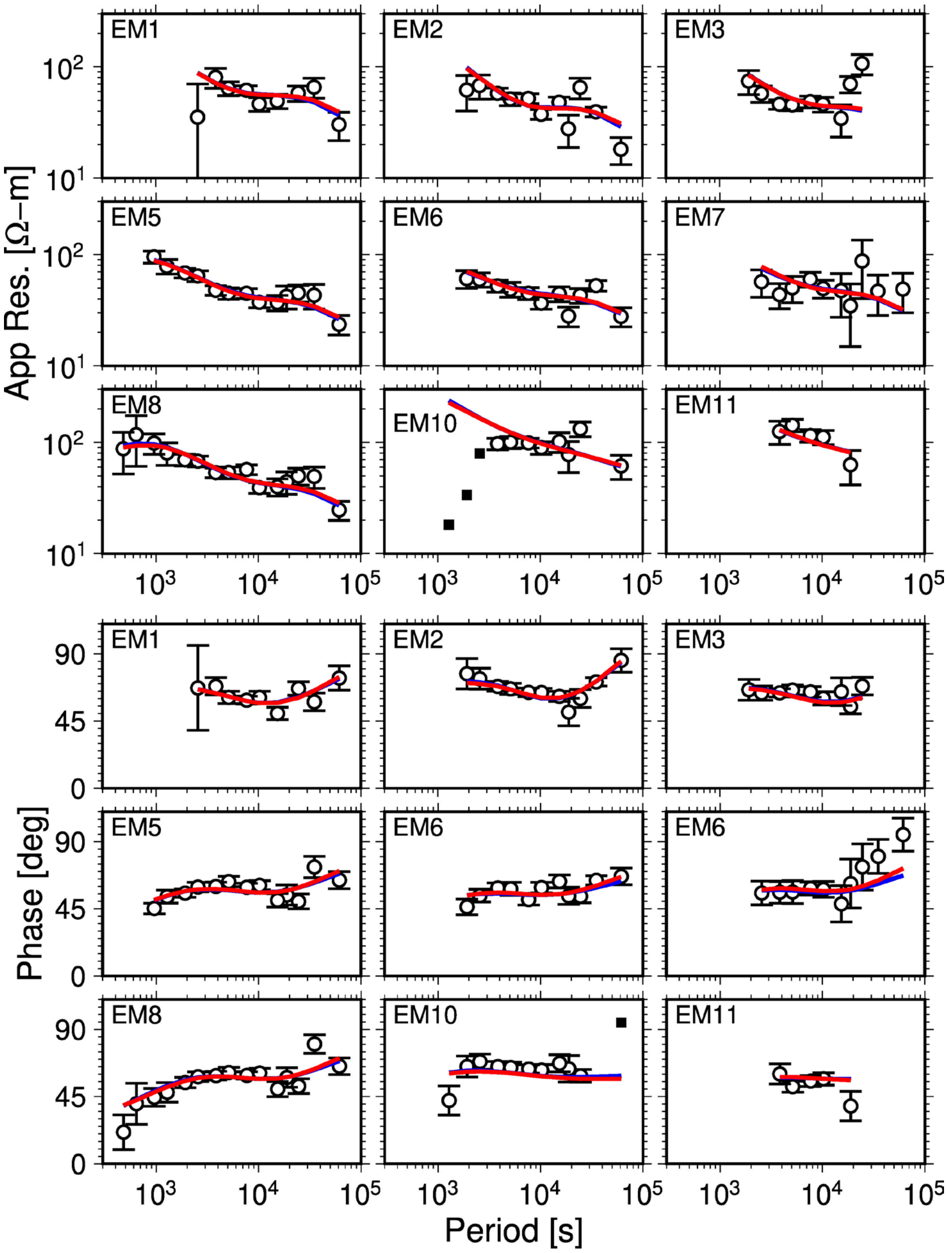

Figure 6

TM mode MT responses observed (circles, with error bar representing one standard error) and predicted from two types of electrical resistivity inversion models (red and blue lines, which correspond to the Figure 5a model and Figure 5b model, respectively). The two lines are almost consistent. The station names are shown in the upper-left corner in each panel. The filled squares seen only in the EM10 response represent outliers that were excluded from the data set by the robust inversion processing. RMS misfits for each site and those for each period are tabulated in Tables S1 and S2, respectively, in the supporting information.

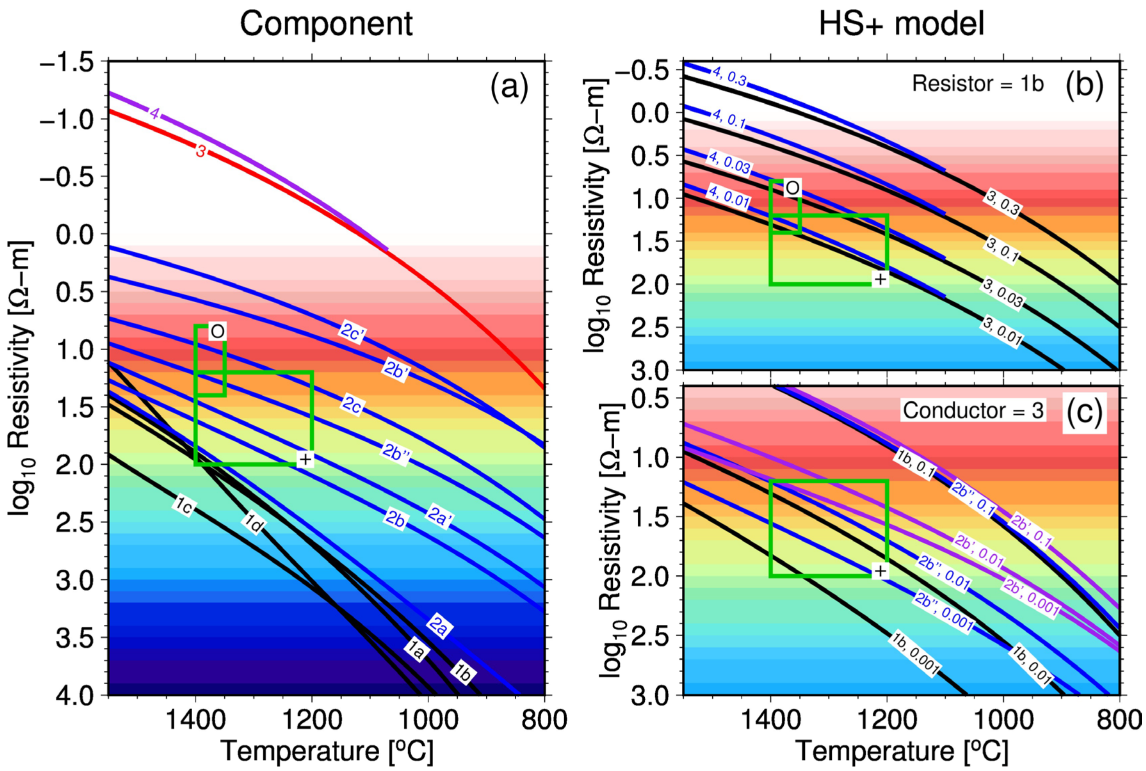

Figure 7

Electrical resistivity as a function of temperature, component, and the amount of melt interconnected in solid phase and water (or hydrogen) dissolved in solid phase or melt. Comparing this figure and the inversion model (Figure 5) with an assumption for temperature of a focusing area, the amount of melt and water (or hydrogen) can be estimated. See details in text.

(a) Electrical resistivity for several types of minerals and materials as a function of temperature, overlying the resistivity color scale used for drawing the inversion models in Figure 5. Black solid lines indicate dry olivine (1a: Yoshino et al., 2009; 1b: Gardés et al., 2014; 1c: Constable et al., 1992; 1d: Constable , 2006). Blue lines indicate wet olivine (2a and 2a': Yoshino et al., 2009 for 0.01 wt.% and 0.1 wt.% water, respectively; 2b, 2b'', and 2b': Gardés et al., 2014 for 0.01 wt.%, 0.03 wt.%, and 0.1 wt.% water, respectively; 2c and 2c': Wang et al., 2006 for 0.01 wt.% and 0.1 wt.% water, respectively). Red line indicates basaltic melt (3) (Tyburczy and Waff, 1983 for tholeiite melt at 4.3 kbar). Purple line indicates hydrous basaltic melt with 1 wt.% water (4) (Sifré et al., 2014). For clarity, the hydrous melt line, 4, is cut at cross-point by the dry silicate melt line, 3. Green boxes with circle or cross indicate resistivity-temperature ranges for areas in the inversion model (Figure 5), which are focused in the discussion section 5.2. in the main text. Boxes with the same symbol are common in Figures 7a, 7b, and 7c.

(b) Electrical resistivity for Hashin-Shtrikman upper bound (HS+) models. The resistor for this figure is the dry olivine of Gardés et al. (2014) (1b in Figure 7a), and the conductors for each line are dry or hydrous basaltic melt (black: tholeiite melt, 3 in Figure 7a; blue: 1 wt.% hydrous melt, 4 in Figure 7a). The melt fraction is written as a decimal number for each line. For clarity, the blue line for hydrous silicate melt, 4, is cut at cross-point by the line for dry silicate melt, 3.

(c) Electrical resistivity for HS+ models. The conductor in this figure is the tholeiite melt of Tyburczy and Waff (1983) (3 in Figure 7a), and the resistors for each line are dry or hydrous olivine (black: dry, 1b in Figure 7a; blue: 0.03 wt.% wet, 2b'' in Figure 7a; purple: 0.1 wt.% wet, 2b' in Figure 7a). The melt fraction is written as a decimal number for each line.

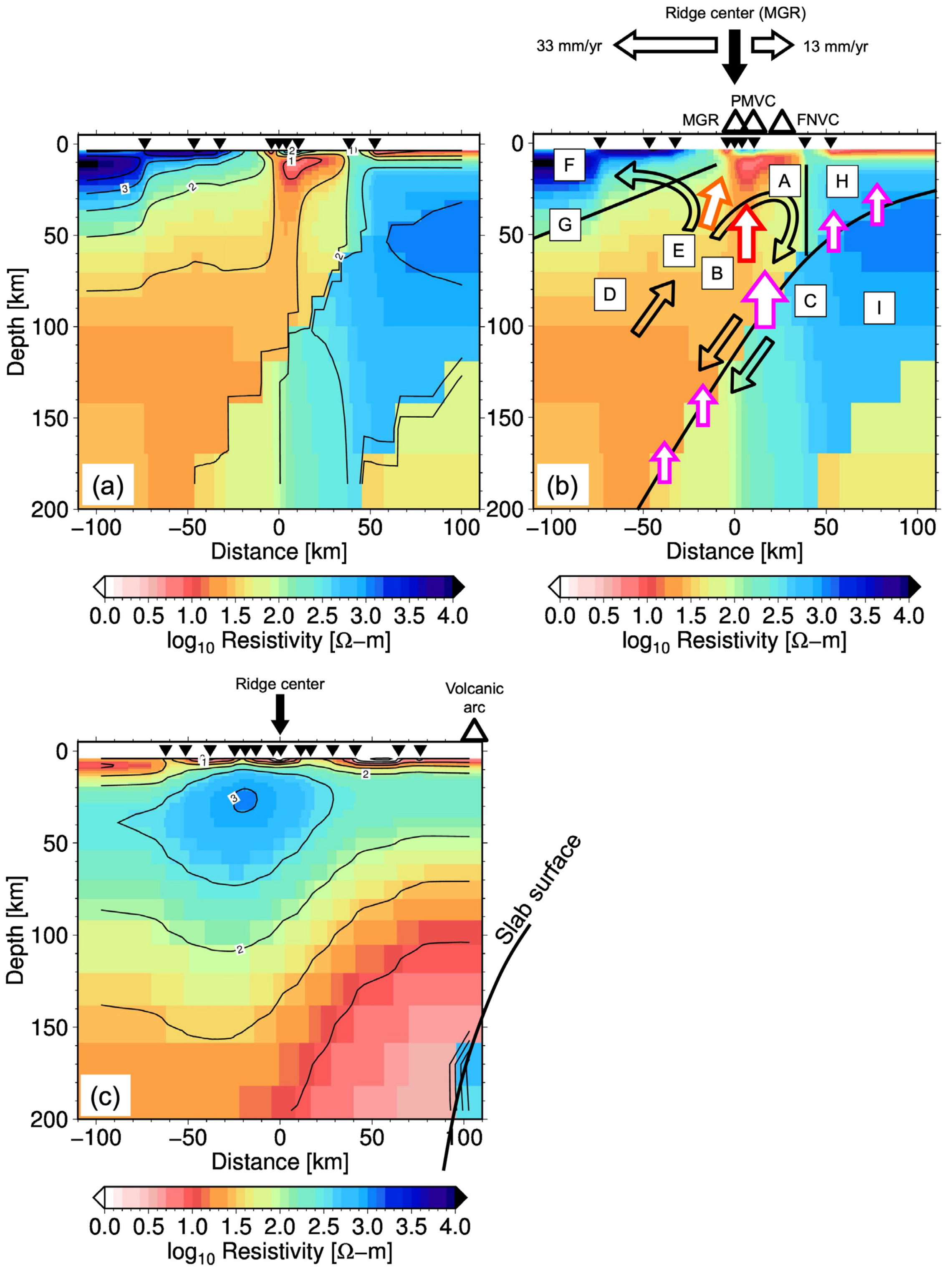

Figure 8

A summary of the interpretations and discussion of the 2-D electrical resistivity model beneath the southern Mariana back-arc spreading ridge at 13°N (Figures 8a and 8b). The background models are the model in Figure 5b. The letters in Figure 8b indicate our model interpretations as follows: A: Melt- and water-rich area, B: Buoyant melt/water upwelling (indicated by the red arrow), C: Slab dehydration, which is significant at ~80-90 km depth (indicated by the magenta arrows), D: Passive, hydrous, asymmetric melting area in an asymmetrically convecting mantle wedge, E: Supply of passive decompression melt (indicated by the orange arrow), F: Depleted and cooled lithospheric mantle, G: Thermal/permeability boundary, H: Cold/serpentinized mantle with some fluid, I: Subducted Pacific slab. The abbreviations in Figure 8b represent as follows: MGR: Malaguana-Gadau Ridge, FNVC: Fina Nagu Volcanic Chain, PMVC: Patgon-Masala Volcanic Chain. The horizontal arrows near the top of Figure 8b indicate seafloor spreading rates at the 13°N segment (Seama and Okino, 2015). Figure 8c is a 2-D inversion model at the central Marianas (Matsuno et al., 2010) for comparison. This central Marianas model is the same as the Figure 6c model in Matsuno et al. (2010). Almost all of the subducted Pacific slab body in the central Marianas lie outside of the plot range of Figure 8c (to the lower right), therefore an outline for the surface of the subducted slab is shown. Contour lines in Figures 8a and 8c are drawn for each $\log_{10}$ Resistivity 0.5.